



1 **Importance of multiple sources of iron for the upper ocean** 2 **biogeochemistry over the northern Indian Ocean**

3 Priyanka Banerjee¹

4 ¹Divecha Centre for Climate Change, Indian Institute of Science, Bangalore, India.

5 *Correspondence to:* Priyanka Banerjee (pbanerjee@iisc.ac.in)

6

7 **Abstract**

8 Although the northern Indian Ocean (IO) is globally one of the most productive regions and receives dissolved
9 iron (DFe) from multiple sources, there is no comprehensive understanding of how these different sources of DFe
10 can impact upper ocean biogeochemical dynamics. Using an Earth system model with an ocean biogeochemistry
11 component this study shows that atmospheric deposition is the most important source of DFe to the upper 100 m
12 of the northern IO, contributing more than 50% of the annual DFe concentration. Sedimentary sources are locally
13 important in the vicinity of the continental shelves and over the southern tropical IO, away from high atmospheric
14 depositions. While atmospheric deposition contributes to more than 10% (35%) to 0-100 m (surface level)
15 chlorophyll concentrations over large parts of the northern IO, sedimentary sources have similar contribution to
16 chlorophyll concentrations over the southern tropical IO. Such increases in chlorophyll are primarily driven by an
17 increase in diatom population over most of the northern IO. The regions that are susceptible to chlorophyll
18 enhancement following external DFe additions are where low levels of background DFe and high background
19 NO₃:DFe values are observed. Analysis of DFe budget over selected biophysical regimes over the northern IO
20 points to vertical mixing as most important for DFe supply, while the importance of advection (horizontal and
21 vertical) varies seasonally. Apart from removal of surface DFe by phytoplankton uptake, subsurface balance
22 between DFe scavenging and regeneration is crucial in replenishing DFe pool to be made available to surface
23 layer by physical processes.

24 **1 Introduction**

25 Iron is an essential micronutrient for primary producers in the ocean due to the catalytic role of iron in
26 photosynthesis, respiration, and nitrogen fixation (Geider & La Roche, 1994; Raven, 1988). Although iron is one
27 of the most abundant elements in the Earth's crust (McLennan, 2001), its low solubility (Sholkovitz et al., 2012)
28 coupled with an intricate balance between complexation by ligands and high scavenging tendency does not make
29 it readily bioavailable (Boyd & Ellwood, 2010). It has been estimated that iron availability limits primary
30 productivity in as much as ~30% of the global oceans, which results in accumulation of unutilized macronutrients
31 like nitrate and phosphate (Moore et al., 2013a). Even in regions experiencing nitrate limitation of productivity,
32 nitrogen fixation is controlled by the supply of iron (e.g., Mills et al., 2004; Moore et al., 2009; Schlosser et al.,
33 2014). Several iron addition experiments performed in the open oceans have demonstrated its significance in
34 regulating phytoplankton growth and drawdown of atmospheric CO₂ (e.g., Blain et al., 2007; Boyd et al., 2007;
35 Coale et al., 1996; de Baar et al., 2005; Pollard et al., 2009).



36 The main external sources of dissolved iron (DFe) to the world oceans are atmospheric depositions (e.g., Conway
37 et al., 2014; Jickells et al., 2005), continental sediments (Elrod et al., 2004; Johnson et al., 1999), river inputs (e.g.,
38 Buck et al., 2007; Canfield, 1997), sea ice (Sedwick & DiTullio, 1997; Wang et al., 2014) and iron seeping from
39 hydrothermal vents (e.g., Nishioka et al., 2013; Tagliabue et al., 2010). Most ocean biogeochemistry models
40 simulating the iron cycle estimate dust ($1.4\text{--}32.7\text{ Gmol yr}^{-1}$) or sedimentary sources ($0.6\text{--}194\text{ Gmol yr}^{-1}$) to have
41 the highest contribution to ocean DFe inventory (Tagliabue et al., 2016). However, many of these models do not
42 include hydrothermal sources of DFe. Numerical modelling using dust, sedimentary and hydrothermal sources of
43 DFe have shown that while ocean column DFe inventory is most sensitive to sedimentary and hydrothermal DFe,
44 atmospheric and sedimentary sources of DFe have the largest impact on atmospheric carbon dioxide (Tagliabue
45 et al., 2014). This is because hydrothermal vents can only impact productivity where these vents are located at
46 shallow depths, while atmospheric and sedimentary DFe can impact productivity over both the open and coastal
47 ocean regions. However, with availability of more *in situ* DFe measurements, the relative importance of different
48 sources of DFe are being re-examined at global as well as regional scales.

49 The northern Indian Ocean (IO) is one of the most productive regions of the global oceans, contributing high
50 levels of organic carbon fluxes to the deeper ocean (e.g., Barber et al., 2001; Madhupratap et al., 2003; Rixen et
51 al., 2019). The monsoonal winds drive phytoplankton blooms over different regions of the northern IO, arising
52 from distinct physical mechanisms in different seasons. These mechanisms include blooms due to coastal and
53 open ocean upwelling, advection of nutrients by ocean currents, and mixed layer deepening by winter convection.
54 Episodic blooms are also triggered by passage of cyclones (Kuttippurath et al., 2021) and mesoscale eddies
55 (Prasanna Kumar et al., 2004; Vidya & Prasanna Kumar, 2013). The region hosts one of the most intense oxygen
56 minimum zones of the world oceans (Schmidtko et al., 2017) and is globally one of the major denitrification sites
57 (e.g., Morrison et al., 1999; Bianchi et al., 2012). Several water column measurements have shown that the primary
58 limiting nutrient over the northern IO is reactive nitrogen with possible colimitation by silicate (Košé et al., 2009;
59 Moore et al., 2013a; Morrison et al., 1998). In recent years, a few studies using ocean biogeochemistry models
60 have also pointed to possible iron limitation of phytoplankton blooms during southwest monsoon months (June-
61 September), especially over upwelling regions of the western Arabian Sea (AS), which is the north-western part
62 of the IO (Košé et al., 2009; Wiggert et al., 2007). These findings on the role of iron limitation have also been
63 supported by incubation experiments over the AS during the late southwest monsoon, which have noted
64 chlorophyll enhancements following iron enrichments (Moffett et al., 2015). Furthermore, *in situ* measurements
65 during the late southwest monsoon have revealed complete drawdowns of silicate, owing to its high utilization
66 under iron limitation, as well as high nitrate-to-iron ratios over the western AS (Naqvi et al., 2010). Nutrient
67 enrichment experiments over the central AS during northeast monsoon months (December-March) have also
68 revealed signatures of iron and nitrate colimitation, with addition of these two nutrients supporting increases in
69 diatoms and coccolithophores (Takeda et al., 1995). Colimitation by nitrogen, phosphorus and iron has been
70 identified over the southern Bay of Bengal (BoB, the north-eastern part of the IO) and the eastern equatorial IO
71 (Twining et al., 2019). Thus, availability of iron can have major impacts on availability of other macronutrients
72 and productivity, which can in turn impact denitrification and mid-depth oxygen levels in this region by
73 modulating fluxes of sinking organic matters.



74 In general, there is a reduction in surface DFe concentrations over the northern IO from north to south. Systematic
75 DFe measurements, encompassing all seasons over the AS, conducted during the Joint Global Ocean Flux Study
76 (JGOFS) of the 1990s showed DFe concentrations often exceeding 1 nM, especially during the southwest
77 monsoon (Measures & Vink, 1999). Subsequent measurements revealed lower levels of DFe with surface values
78 ranging between 0.2-1.2 nM over the AS and between 0.2-0.5 nM over the BoB (Chinni et al., 2019; Chinni &
79 Singh, 2022; Grand et al., 2015; Moffett et al., 2015; Vu & Sohrin, 2013). These values are generally higher than
80 most of the open ocean regions. In contrast, southwards of the equatorial IO have surface DFe values generally
81 less than 0.2 nM (e.g., Chinni et al., 2019; Grand et al., 2015; Twining et al 2019; Vu & Sohrin, 2013). The oxygen
82 minimum zone, located to the north of the equator between depths of 150-1000 m, has elevated levels of DFe (>1
83 nM), possibly due to DFe transport from reducing shelf sediments and remineralization of sinking organic matter
84 (Moffett et al., 2007).

85 The overall high values of DFe over the northern IO can stem from multiple external sources of DFe identified
86 within this region: atmospheric aerosol inputs (dust and black carbon) from South and Southwest Asia (Banerjee
87 et al., 2019; Srinivas et al., 2012), continental shelf sediments, high river discharge, especially, over the BoB (e.g.,
88 Chinni et al., 2019; Grand et al., 2015) and hydrothermal vents from the Central Indian Ridge that mainly impact
89 DFe levels at depths of around 3000 m (Nishioka et al., 2013). The importance of episodic dust depositions in
90 alleviating iron limitations of primary productivity over the central AS has been identified, during the northeast
91 monsoon when a deeper ferricline compared to the nitracline yields a high nitrate-to-iron ratio (Banerjee and
92 Kumar, 2014). Additionally, modelling studies over the AS have demonstrated that DFe derived from dust
93 deposition can support about half of the observed primary productivity and a large fraction of nitrogen fixation
94 (Guieu et al., 2019). Centennial-scale model simulations over the IO have revealed that changes in phytoplankton
95 community structure have resulted in increased (reduced) carbon uptake over the eastern (western) IO in response
96 to increased anthropogenic DFe deposition in the present day compared to pre-industrial levels (Pham & Ito,
97 2021). Yet another challenge is that, away from regions with high aerosol loading, other sources of DFe can
98 become important in supporting ocean productivity and controlling patterns of nutrient limitations. Such
99 understanding of relative roles of different sources of DFe in controlling the biogeochemical dynamics of the
100 northern IO remains unexplored. This is important considering the multiple sources of DFe over the northern IO.
101 To this end, the present study uses a suite of simulations from a state-of-the art Earth system model with an iron
102 cycle in its ocean biogeochemistry component to explore the relative contribution of different sources of DFe to
103 phytoplankton blooms and impacts on nutrient availability over the upper 100 m of the northern IO. Furthermore,
104 DFe budget has been analysed over the upper ocean for varied biophysical regimes in this region to identify how
105 different sources of DFe can impact the total DFe budget.

106

107 **2 Data and model**

108 The study uses satellite and reanalysis products, ocean observation data, and an Earth system model to assess
109 contributions of different sources of DFe to phytoplankton blooms over the northern IO. For the present study,
110 the northern IO is considered to encompass 30°N–20°S latitude, 40°–105°E longitude. Thus, the tropical part of
111 the southern IO is also included. Only the open ocean regions, having bottom depth greater than 1000 m, are
112 studied here. The four seasons referred to in this study are defined as: the northeast monsoon: December-March;



113 spring intermonsoon: April-May; southwest monsoon: June-September; and fall intermonsoon: October-
114 November.

115 **2.1 Model**

116 This study uses the ocean component Parallel Ocean Program version 2 (POP2) (Smith et al., 2010) embedded in
117 the Community Earth System Model (CESM) version 2.1. This version of CESM incorporates several
118 improvements over previous versions of the model (Danabasoglu et al., 2020). The POP2 model is a level-
119 coordinate model having Arakawa B-grid in the horizontal with North Pole displaced over Greenland. The vertical
120 resolution is 10 m for the upper 160 m and decreases with depth to 250 m in the bottom. The horizontal resolution
121 is nominally 1° with meridional resolution increasing to 0.27° near the equator (Danabasoglu et al., 2012),
122 implying that mesoscale eddies are not resolved. Momentum advection is based on a second-order central
123 advection scheme while tracer advection relies on a third-order upwind advection scheme. Vertical ocean mixing
124 is parameterized using the non-local K-Profile parameterization (Large et al., 1994), which is incorporated into
125 CESM2.1 via the Community Ocean Vertical Mixing (CVMix) framework. Horizontal mixing is parameterized
126 using the Gent and Williams (1990) scheme, which includes eddy-induced velocity in addition to diffusion of
127 tracers along isopycnals. Macronutrients and oxygen are initialized from World Ocean Atlas 2013 version 2
128 dataset (Garcia et al., 2014a, b) and alkalinity is initialized using GLObal Ocean Data Analysis Project
129 (GLODAPv2; Olsen et al., 2016).

130 The biogeochemistry component of POP2 is implemented using Marine Biogeochemistry Library (MARBL),
131 which is the most updated version of the previously implemented Biogeochemistry Elemental Cycle (BEC) model
132 (Long et al., 2021). The model includes key limiting nutrients (N, P, Si, Fe), three types of explicit phytoplankton
133 functional groups (diatoms, diazotrophs and nano/picophytoplankton), one implicit calcifier group, and one
134 zooplankton type. The C:N ratio for nutrient assimilation is fixed at 117:16 (Anderson and Sarmiento, 1994),
135 whereas P:C, Fe:C, Si:C and chlorophyll:C ratios are allowed to vary based on ambient nutrient concentrations.
136 The Fe:C ratio is allowed to change within a fixed range based on phytoplankton growth terms, loss terms, and
137 the iron uptake half-saturation constant for different phytoplankton groups (Moore et al., 2004). For each of the 3
138 phytoplankton groups the minimum allowed Fe:C ratio is 2.5 $\mu\text{mol mol}^{-1}$. The maximum allowed Fe:C ratio is 30
139 $\mu\text{mol mol}^{-1}$ for diatoms and small phytoplankton, and 60 $\mu\text{mol mol}^{-1}$ for diazotrophs due to their higher demand
140 for iron. The zooplankton Fe:C ratio is fixed at 3.0 $\mu\text{mol mol}^{-1}$. Individual nutrient limitation for phytoplankton is
141 assessed based on Michaelis-Menten nutrient uptake kinetics, which is a function of the specific nutrient
142 concentration and nutrient uptake half-saturation coefficient. The half-saturation coefficient is nutrient-specific
143 and phytoplankton-group specific. Nutrient limitation terms vary from 0 to 1, with 0 being the most limiting
144 nutrient. Multiple nutrient limitation follows Liebig's law of minimum, so that the nutrient limitation term with
145 minimum value limits phytoplankton growth rate (Long et al., 2021). Loss of phytoplankton in MARBL is
146 accounted for by grazing, mortality, and aggregation of sinking flocculants.

147 The main DFe sources considered in MARBL are atmospheric depositions, shelf sediments, riverine inputs, and
148 hydrothermal vents. Globally, these sources of DFe account for 13.62 Gmol yr^{-1} , 19.68 Gmol yr^{-1} , 0.37 Gmol yr^{-1} ,
149 and 4.91 Gmol yr^{-1} , respectively (Long et al., 2021). Atmospheric sources of DFe are from dust and black carbon
150 depositions obtained from a fully coupled CESM2 simulation in hindcast mode at nominal 1° spatial resolution as



151 a part of the Coupled Model Intercomparison Phase 6 (CMIP6) contribution. Dust emissions and
152 transport/deposition are calculated, respectively, using the Community Land Model version 5 (CLM5) and
153 Community Atmosphere model version 6 (CAM6) in Whole Atmosphere Community Climate Model (WACCM)
154 configuration. The newly included Modal Aerosol Module version 4 (MAM4) in CAM6 includes dust in the
155 accumulation and coarse modes. Black carbon is emitted in the primary mode and transferred to accumulation
156 mode via aging (Liu et al., 2016). Monthly climatology of dust and black carbon for the year 2000 is used in
157 repeating mode. About 3.5% of dust is assumed to be iron with the solubility of iron depending on the ratio
158 between coarse and fine dust fluxes. This accounts for increasing iron solubility with increasing distance from
159 dust source regions. A constant solubility of 6% is assigned to iron derived from black carbon aerosols.
160 Sedimentary iron supply is based on sub-grid scale bathymetry that depends on two factors: firstly, for reducing
161 sediments, it is proportional to particulate organic carbon fluxes in regions where these fluxes are larger than 3 g
162 $\text{C m}^{-2} \text{ yr}^{-1}$; secondly, in oxic sediments, it depends on constant low background fluxes and bottom current velocity,
163 which accounts for sediment resuspension. As a result, the main sources of sedimentary DFe are along continental
164 shelves and productive margins, with little contribution coming from the deep ocean. For the river source of DFe,
165 discharge data for the year 2000 from Global Nutrient Export from WaterSheds (GlobalNEWS, Mayorga et al.,
166 2010) is combined with constant DFe concentration of 10 nM. For hydrothermal vents, a constant flux of iron
167 from the grid boxes containing vents is applied so that the total hydrothermal vent iron flux is equal to
168 approximately 5.0 Gmol yr^{-1} .

169 Iron input to oceans is balanced by losses from biological uptake and scavenging. Loss of iron from the biological
170 pool occurs through mortality and grazing upon phytoplankton by zooplankton as well as higher trophic grazing
171 on zooplankton. In CESM, scavenging increases non-linearly with DFe concentration. The scavenging rate
172 depends on the total sinking fluxes of particulate organic carbon, biogenic silica, calcium carbonate and dust,
173 which strongly influence DFe in excess of ligand concentrations (Moore and Braucher, 2008). Scavenged iron
174 enters the particulate iron pool, while iron released from grazing and mortality of autotrophs and zooplankton also
175 contributes to the particulate iron pool depending on species-specific Fe:C ratios. Remineralization of particulate
176 iron at depth is parameterized as a function of the particulate organic carbon flux. Desorption of iron contributes
177 to the remineralized iron pool and is calculated using a constant desorption rate for scavenged iron. In addition,
178 there is slow dissolution of “hard” dust fraction (~98% of total dust) with depth such that ~0.3% of dust will
179 dissolve over 4000 m (Armstrong et al., 2002; Moore et al., 2004). For the remainder of the 2% “soft” dust,
180 remineralization takes place with a length-scale of 200 m. The model also includes an explicit ligand tracer for
181 complexing Fe, with ligand sources being from particulate organic carbon remineralization and dissolved organic
182 matter production. Ligand sinks are scavenging, uptake by phytoplankton, ultraviolet radiation, and bacterial
183 uptake or degradation.

184 This study is based on 5 sets of simulations for identifying contributions from different sources of DFe: control
185 simulation (CTRL); and simulations that individually remove DFe supply from atmospheric depositions (NATM),
186 sediments (NSED), rivers (NRIV) and hydrothermal vents (NVNT). Differences between CTRL and NATM
187 simulations indicate the biogeochemical impacts solely due to atmospheric deposition of DFe and is referred to
188 as ATM. Similarly, biogeochemical impacts solely from sedimentary, river and hydrothermal DFe sources are,
189 respectively, referred to as SED, RIV and VNT cases. Simulations have been conducted in hindcast mode for 60



190 years using forcing from the Coordinated Ocean-ice Reference Experiments version 2 (CORE-II) dataset for the
191 years 1948-2007 (Large & Year, 2009). The CORE-II data includes interannual variability and consists of 6-
192 hourly temperature, air density, specific humidity, 10 m wind-speeds, and sea-level pressure from National
193 Centers for Environmental Prediction/ National Center for Atmospheric Research (NCEP/NCAR) Reanalysis
194 (Kalnay et al., 1996). Daily shortwave and longwave radiation are taken from Goddard Institute for Space Studies-
195 International Satellite Cloud Climatology Project radiative flux profile data (GISS-ISCCP-FD) (Zhang et al.,
196 2004). Monthly precipitation is combined Global Precipitation Climatology Project (GPCP, Huffman et al., 1997)
197 and Climate Prediction Center Merged Analysis of Precipitation (CMAP, Xie & Arkin, 1997) data. Monthly
198 streamflow since 1948 is based on gauge data and CLM model has been used to calculate the freshwater fluxes
199 (Dai et al., 2009). The present study uses the last 10 years of simulations, given its focus on impacts of DFe
200 sources on biogeochemistry of the upper 100 m of the oceans at seasonal scale.

201 2.2 Observation data

202 Monthly climatology for ocean temperature, salinity and nutrients have been obtained from World Ocean Atlas
203 2018 (WOA18) at $1^{\circ}\times 1^{\circ}$ spatial resolution (Garcia et al., 2019). Monthly surface chlorophyll concentrations have
204 been obtained from the European Space Agency Ocean Color Climate Change Initiative (OC-CCI) version 5 at 4
205 km spatial resolution for the period 2003-2020 (Satyendranath et al., 2019). OC-CCI merges ocean color
206 information from multiple sensors: Moderate Resolution Imaging Spectroradiometer (MODIS, 2002-present),
207 Sea-Viewing Wide Field-of-View Sensor (SeaWiFS, 1997-2010), MEdium Resolution Imaging Spectrometer
208 (MERIS, 2002-2012) and Visible Infrared Imaging Radiometer (VIIRS, 2012-present). The product is bias-
209 corrected and quality-controlled, yielding much lower data gaps compared to individual sensors. Monthly
210 climatology of mixed layer depth (MLD) gridded at $1^{\circ}\times 1^{\circ}$ spatial resolution has been obtained from Argo profiles
211 based on a hybrid algorithm that calculates a suite of MLDs using several criteria, such as gradient/threshold
212 method, maxima or minima of a particular property, intersection with seasonal thermocline (Holte et al., 2017).
213 The resulting patterns are analysed to yield final MLD estimates. To explore ocean surface circulation, Ocean
214 Surface Current Analysis Real-time (OSCAR) data at $0.33^{\circ}\times 0.33^{\circ}$ spatial resolution and 5-day temporal resolution
215 has been used. Horizontal velocities are measured using sea surface heights, ocean surface winds, and sea surface
216 temperatures, thereby accounting for flows due to geostrophic balance, Ekman dynamics, and thermal wind
217 (Dohan & Maximenko, 2010).

218

219 To examine the ability of CESM to realistically simulate the variation in DFe concentrations in the upper 100 m
220 over the northern IO, this study uses DFe profile compilations by Tagliabue et al. (2012) and the GEOTRACES
221 Intermediate Data Product 2021 (Schlitzer et al., 2021). To these, published data from Moffett et al. (2015) has
222 also been added, comprising DFe data collected in the AS during September 2007. The DFe estimated in these
223 data are based on filtration of seawater through filter sizes between 0.2-0.45 μm .

224

225 3 Results and discussions

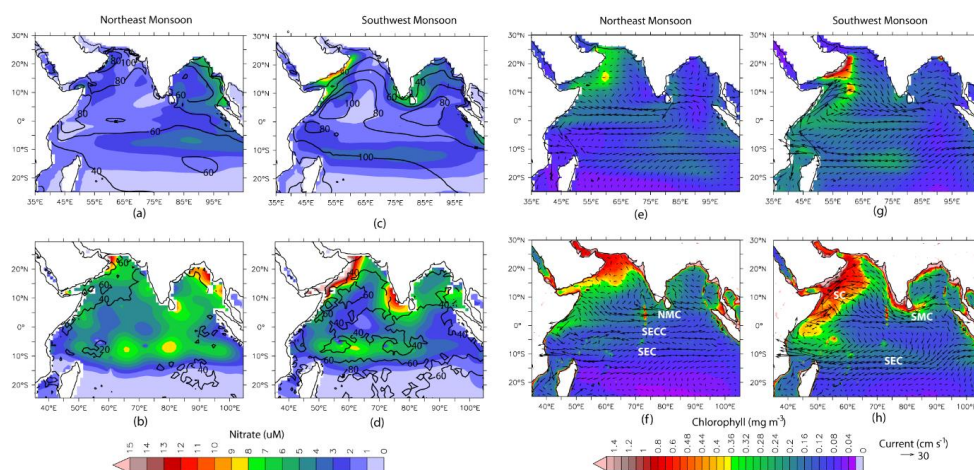
226 First, the performance of CESM-POP2 simulations with respect to observations over the northern IO is examined.
227 Next, the contributions of different DFe sources to upper ocean DFe concentrations, phytoplankton blooms and
228 patterns of nutrient limitations is discussed. Finally, the paper explores how different sources of DFe can influence
229 the total DFe budget across selected biophysical regimes over the northern IO.



230 3.1 Model evaluation

231 In this section CESM simulation (for CTRL case) of physical parameters as well as nitrate and chlorophyll
232 concentrations over the upper 100 m of the northern IO is evaluated. Except for MLD, ocean currents, and
233 chlorophyll, all modeled parameters have been compared with WOA18 observations. Simulated MLDs are
234 compared with Argo-based values of Holte et al. (2017), ocean currents are compared with OSCAR data, and
235 chlorophyll concentrations are compared with OC-CCI observations. In general, CESM shows good
236 correspondence with observations of seasonal cycle of temperature, salinity and MLD. However, there is positive
237 temperature and salinity bias over IO (Figs. S1 and S2 in the Supplement). This warm bias over IO differs from
238 the previous version of CESM, which has a cold bias in this region (Danabasoglu et al., 2020). Figure 1 shows
239 seasonal climatology in CESM simulations and observations, for MLD, nitrate concentrations, surface ocean
240 currents, and chlorophyll concentrations. Overall, CESM simulates the main features of surface ocean circulation
241 and spatio-temporal variations in MLD well. There are some deviations, such as a much stronger simulated Somali
242 Current along the northeast coast of Africa, especially during the southwest monsoon season, which can lead to
243 strong advection of upwelled nutrients away from this region. CESM also simulates a stronger South Equatorial
244 Current during southwest monsoon, which occupies a broader region compared to observations and leads to a
245 stronger westward flow in the model between 0-5°S latitude. The net result of the warm and positive salinity bias
246 is that CESM simulates much deeper MLD than observations throughout the year across the study domain.
247 Averaged annually, the largest overestimation (of ~40 m) is over the equatorial IO particularly during the spring
248 and fall intermonsoon months, when the Wyrтки Jet is prevalent over the region (Figs. S2 e-f). Additionally, MLD
249 overestimation of ~45 m is also seen over the AS during February-March and the southern tropical IO during
250 September-October, both associated with winter-convection.

251 With respect to the seasonal cycle of nitrate, CESM has the least bias over AS followed by BoB (Figs. 1a-d and
252 S3), but its performance is comparatively lower over the equatorial IO and southern tropical IO. For example,
253 WOA18 data shows the highest value of nitrate over southern tropical IO in January, whereas in CESM simulation
254 the highest nitrate concentration is shifted to April-June associated with mixed layer deepening. On the other
255 hand, CESM simulates a much weaker seasonal cycle of nitrate over the equatorial IO compared to WOA18
256 observations. These regions, over southern tropical IO and the equatorial IO, where CESM fares poorly also have
257 fewer nutrient profile observations compared to AS and BoB. For example, no more than 10 nitrate observations
258 are available in a grid-point over the southern tropical IO and equatorial IO, whereas there are several grid-points
259 over the AS where more than 30 observations are available. Overall, CESM simulations underestimate nitrate
260 with respect to WOA18 data for the upper 100 m of the water column.



261

262 **Figure 1: Comparison of CESM-CTRL simulated variables (upper panels) with observations (lower panels) for**
 263 **northeast monsoon (a,b,e,f) and southwest monsoon (c,d,g,h). Shading in (a-d) are nitrate concentrations averaged for**
 264 **upper 100 m and the black contours are the mixed layer depth (m). Shading in (e-h) are surface chlorophyll**
 265 **concentrations and the vectors are the surface currents. SEC: South Equatorial current, SECC: South Equatorial**
 266 **Counter Current, NMC: Northeast Monsoon Current, SMC: Southwest Monsoon Current, SC: Somali Current.**

267

268 Turning to chlorophyll concentrations, CESM simulations capture the main characteristics of the seasonal cycle
 269 and its spatial distribution over the northern IO (Figs. 1e-h and S3), with certain biases and shifts in the timing of
 270 the peak blooms. For example, over the BoB, the model has difficulty in capturing the temporal evolution of
 271 chlorophyll concentrations. Over the AS and the equatorial IO, peak bloom in the simulations occurs in September,
 272 in contrast to July in the observations. Similarly, over the southern tropical IO, the peak bloom is delayed in the
 273 model to October as compared to its appearance in July in observations. Most of the AS and the BoB show
 274 underestimation (~ -60%) in simulated chlorophyll concentration with respect to OC-CCI values. Such
 275 underestimation of major nutrients and chlorophyll over most of the northern IO are common to many modelling
 276 studies where coastal regimes and mesoscale processes are not adequately captured without finer spatial resolution
 277 (e.g., Dutkiewicz et al., 2012; Ilyina et al., 2013; Long et al., 2021; Moore et al., 2013b; Pham & Ito, 2021). For
 278 example, a modelling study by Resplandy et al. (2011) has shown that eddy-induced vertical transport is
 279 responsible for ~40% of nitrate fluxes in the winter convection regions of the AS during the late northeast
 280 monsoon. The study also showed that mesoscale eddies can account for 65-91% of vertical and lateral advection
 281 of nitrate in the upwelling regions of the AS during the southwest monsoon. Additionally, the positive MLD bias
 282 simulated by CESM can trigger light limitation of phytoplankton growth, leading to underestimation of
 283 chlorophyll. If the threshold depth for photosynthesis is considered as the depth of the isolume given by 0.415
 284 mol quanta m⁻² day⁻¹ (Z_{0.145}, Boss & Behrenfeld, 2010; Letelier et al., 2004), then the CESM simulated MLD is
 285 deeper than the Z_{0.145}, leading to light limitation of phytoplankton growth over the entire AS and large parts of
 286 BoB throughout the year (Fig. S4). During the southwest monsoon, almost the entire domain experiences light
 287 limitation, especially off the coast of Somalia and the southern tropical IO.

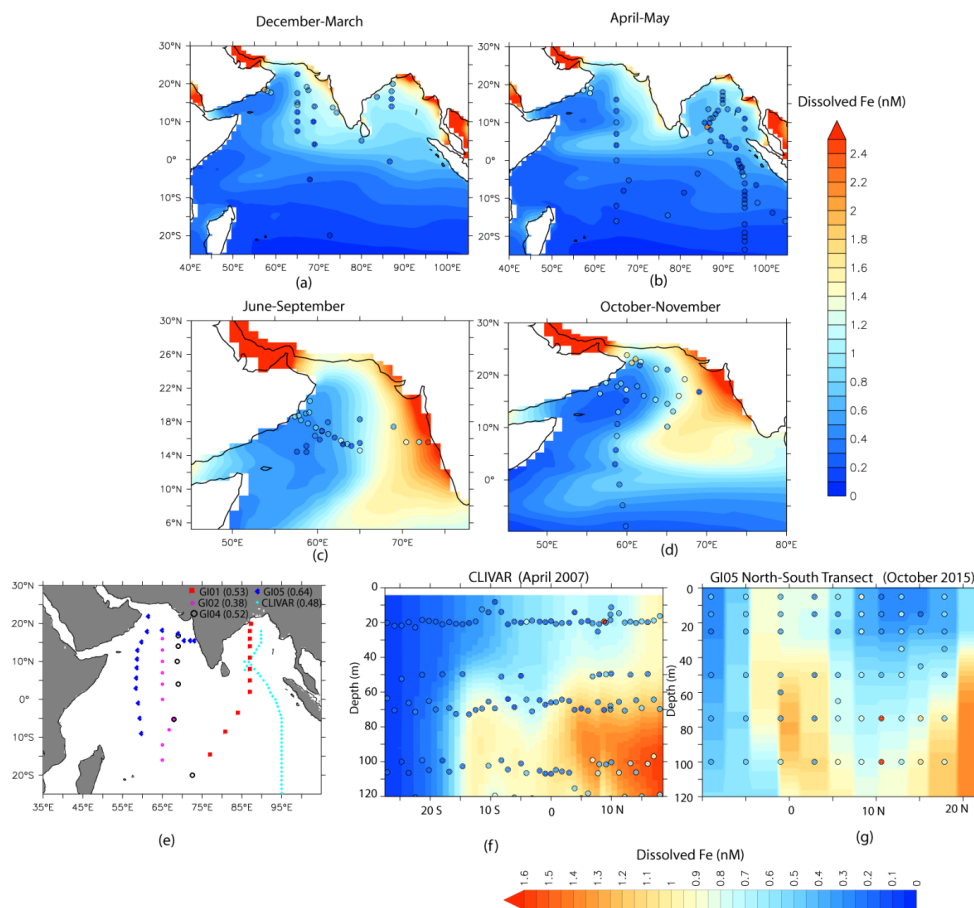
288 CESM simulations of DFe are evaluated next, using all available *in situ* DFe concentration data for upper 20 m
 289 of the ocean, for different seasons. In addition, distribution of DFe along selected transects for the upper 100 m



290 are studied: (1) CLIVAR cruise 109N along the eastern IO during April 2007; and (2) GEOTRACES cruises GI-
291 01, GI-02, GI-04 and GI-05. While CESM simulates the general pattern of DFe distribution over the northern IO
292 reasonably well, DFe variation with depth and with increasing distance from the coast is stronger in simulations
293 than in observations. For upper 20 m, correlation between observed and simulated DFe concentrations is 0.41
294 (Figs. 2a-d). The coefficients for correlation between observed and simulated DFe for GEOTRACES and
295 CLIVAR transects vary between 0.64 and 0.38 (Fig. 2e). All these correlation coefficients are significant at 95%
296 confidence level. This indicates that CESM is able to reproduce the north-to-south gradient in DFe concentrations,
297 the comparatively low DFe concentration west of 65°E over the AS, as well as increases in DFe with depth over
298 both the eastern and western IO reasonably well.

299 Figures 2 f and g show two examples of variation of DFe distribution with latitude and depth along the eastern
300 and western IO, respectively. The model overestimates DFe values, especially to the north of the equator and at
301 depths greater than 50 m. Such overestimation of DFe over the northern IO in CESM could result from a variety
302 of factors, like source strength, assumed solubility of iron, biases in dissolved oxygen concentrations or ligand
303 concentrations, and uncertainties in the removal of DFe by biological uptake as well as scavenging. Specific
304 attribution for the overestimation of simulated DFe is beyond the scope of this paper. Dust deposition is one
305 possible factor leading to overestimation of simulated DFe. However, due to sparse dust deposition observations
306 available over this region, it is difficult to come to conclusion about its role in CESM-simulated DFe bias over
307 this region. Using Dust Indicators and Records of Terrestrial and MARine Palaeoenvironments (DIRTMAP)
308 version 2 database of modern day dust deposition (Kohfeld & Harrison, 2001) an attempt has been made here to
309 understand CESM bias in dust deposition over AS. Median dust deposition values from DIRTMAP ranges
310 between $\sim 14 \text{ g m}^{-2}\text{yr}^{-1}$ over the western AS (40°-60°E), $\sim 7 \text{ g m}^{-2}\text{yr}^{-1}$ over the central AS (60°-70°E) and $\sim 20 \text{ g m}^{-2}\text{yr}^{-1}$
311 $\sim 2 \text{ g m}^{-2}\text{yr}^{-1}$ over the eastern AS (70°-80°E) (Kohfeld & Harrison, 2001). Corresponding median values of dust deposition
312 over these locations from CESM model are $5 \text{ g m}^{-2}\text{yr}^{-1}$, $9 \text{ g m}^{-2}\text{yr}^{-1}$ and $14 \text{ g m}^{-2}\text{yr}^{-1}$ respectively. It is important to
313 note here that DIRTMAP represent dust depositions estimates for a specific location using a wide range of
314 methods, while CESM depositions are averaged over $\sim 100 \text{ km}$. Over the eastern IO, using mixed layer dissolved
315 Al concentrations dust depositions have been estimated to be $0.2\text{-}3.0 \text{ g m}^{-2}\text{yr}^{-1}$ between 20°S to 10°N latitude
316 (Grand et al., 2015). In a separate study, based on Al concentrations in the aerosol, Srinivas and Sarin (2013) have
317 estimated dust dry-deposition flux of $0.3\text{-}3.0 \text{ g m}^{-2}\text{yr}^{-1}$ over BoB. Dust deposition from CESM is on the lower end
318 of this range varying from $1.1 \text{ g m}^{-2}\text{yr}^{-1}$ over the northern BoB to $0.2 \text{ g m}^{-2}\text{yr}^{-1}$ near the equator. Sediment traps
319 deployed at shallow depths over the BoB have recorded annual lithogenic fluxes varying from the northern to the
320 southern bay as $\sim 15 \text{ g m}^{-2}\text{yr}^{-1}$ ($\sim 89.5^\circ\text{E}$, 17.5°N) to $\sim 4 \text{ g m}^{-2}\text{yr}^{-1}$ (87°E , 5°N) (Unger et al., 2003). The corresponding
321 variations in CESM dust deposition are $\sim 9 \text{ g m}^{-2}\text{yr}^{-1}$, to $\sim 2 \text{ g m}^{-2}\text{yr}^{-1}$. Thus, overall, there is possibly some
322 underestimation of dust deposition over the northern IO, which might not explain positive DFe bias in CESM
323 simulations. Due to unavailability of measurements, it is very difficult to quantify the importance of other sources
324 of DFe in contributing to positive DFe bias in CESM simulations.

325



326

327 **Figure 2: Comparison of CESM-CTRL simulated DFe (shading) with the observations (filled circles) compiled from**
 328 **various cruises. The spatial distribution maps in (a-d) consider season-wise DFe distribution averaged over the upper**
 329 **20 m. (e) The different cruise tracks from which DFe measurements have been marked. The numbers within**
 330 **the parentheses are the correlation coefficients between observed and simulated DFe for each cruise. The vertical**
 331 **transects in (f-g) show DFe gradients in the water column over (f) the eastern Indian Ocean and (g) the western Indian**
 332 **Ocean.**

333

334 It is seen that CESM consistently overestimates dissolved oxygen over the northern IO with respect to the WOA18
 335 concentrations (Fig. S5). This implies that overestimation of sub-surface DFe concentrations in the model does
 336 not originate in the magnitude and the spatial extent of poorly oxygenated sub-surface waters. The impact of
 337 organic ligands in maintaining DFe stock by preventing scavenging losses can introduce yet another notable
 338 source of bias in simulated DFe. Only one study has measured ligand concentrations over the northern IO, during
 339 the spring intermonsoon of 1995 (Witter et al., 2000). At 100 m depth, observed ligand concentration ranges from
 340 1.47 nM over the western AS to 4.94 nM over the eastern AS. The corresponding values from CESM simulations
 341 range from 1.55 nM in the western AS to 1.19 nM over the eastern AS. However, it is not possible to conclude
 342 about the impact of ligands on simulated DFe biases based on a single study. With respect to scavenging losses,
 343 it is quite possible that underestimation of productivity over the northern IO can lead to corresponding bias in



344 scavenging losses. This is because the base scavenging rate in CESM, apart from depending on dust fluxes, is also
345 a function of sinking fluxes of particulate organic matter, biogenic silica, and calcium carbonate. For example,
346 averaged over a year, there is ~60% underestimation in CESM of surface chlorophyll concentrations over the
347 northern IO, which would impact the sinking fluxes of biogenic matter. This can reduce scavenging losses,
348 especially, when there is a likely underestimation of dust deposition by CESM. Underestimation of phytoplankton
349 biomass over the northern IO can also lead to underestimation of phytoplankton uptake losses of DFe in the upper
350 100 m, which can be yet another source of overestimation of DFe.

351 To summarize, the ocean component of CESM model has deeper MLD than observations, underestimates nitrate
352 and chlorophyll and overestimates DFe concentrations. It is difficult to come to a definitive conclusion regarding
353 the importance of source strength in explaining the positive bias in DFe. It is quite possible that underestimation
354 of scavenging losses of excess DFe and biological uptake play vital roles in explaining positive DFe biases in this
355 region. Still, the model simulates spatial and temporal patterns of ocean physical features, as well as variations in
356 chlorophyll concentrations, nitrate, and DFe concentrations over the northern IO reasonably well. This gives
357 confidence in using the model to study the iron cycle over the region. Taking the above understanding of strengths
358 and shortcomings of the model into account, the importance of different DFe sources with respect to
359 biogeochemistry of the upper 100 m of the northern IO is explored next.

360

361 3.2 Contribution of multiple iron sources

362

363 Figure 3 summarizes the contributions of different sources to annually averaged DFe concentration. Source-wise
364 DFe contributions for northeast and southwest monsoons are shown in Figs. S6 and S7 respectively. Overall, the
365 relative contribution from different sources to DFe is roughly the same across different seasons, except for the
366 somewhat higher contribution of atmospheric DFe during southwest monsoon compared to northeast monsoon.
367 This is because the arid and semi-arid regions surrounding the northern IO experiences maximum dust activity
368 from late spring to early southwest monsoon months (e.g., Banerjee et al., 2019; Léon and Legrand, 2003). In the
369 annual average, atmospheric deposition is the most important source of DFe over the northern IO and contributes
370 well above 50% of the total DFe concentrations (ATM case in Fig. 3b). Furthermore, atmospheric deposition
371 contributes more than 70% of DFe supply over most of the AS, southern BoB, and the equatorial IO. The location
372 of the intertropical convergence zone during northeast monsoon (~10°S latitude) determines the southern limit of
373 the influence of atmospheric deposition because southwards of the intertropical convergence zone there is a rapid
374 reduction in DFe concentrations. Dust is the predominant contributor to the atmospheric deposition flux of iron.
375 Over the northern AS, dust is mostly transported from Iran, Pakistan, Afghanistan, and the Arabian Peninsula,
376 whereas over southern AS dust from north-eastern Africa also becomes important (Jin et al., 2018; Kumar et al.,
377 2020). Over northern and southern BoB, the major sources of dust are the Indo-Gangetic Plain and northeast
378 Africa, respectively (Banerjee et al., 2019). Eastwards of 90°E, black carbon contributes ~50% to atmospheric
379 DFe flux during the northeast monsoon (not shown). The source of black carbon in this region is biomass burning
380 and fossil fuel combustion transported from the Indo-Gangetic Plain and Southeast Asia (Gustafsson et al., 2009;
381 Moorthy & Babu, 2006).

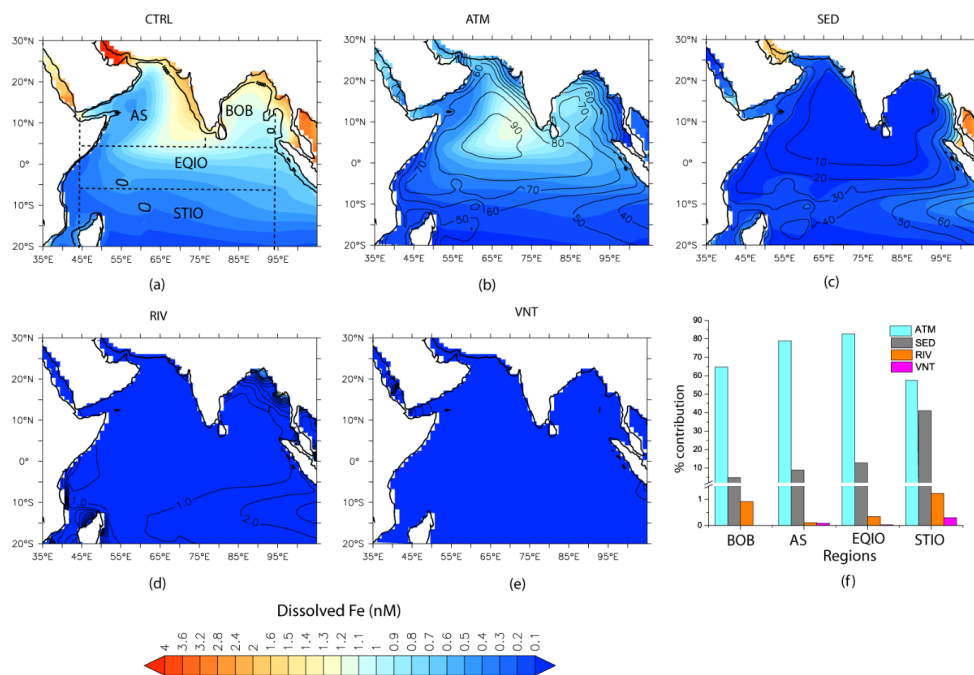


382 The second largest source of DFe is from continental shelf sediments (Fig. 3c), which become dominant in the
383 vicinity of the shelves. High sedimentary sources of DFe are characteristic of the Andaman Sea where incoming
384 rivers can contribute $\sim 600 \times 10^6 \text{ T yr}^{-1}$ of sediments (Robinson et al., 2007). It has been estimated that terrestrial
385 sources contribute more than 80% to total organic carbon in the inner shelf region of the Gulf of Martaban,
386 adjacent to the Andaman Sea (Ramaswamy et al., 2008). Elsewhere, sedimentary contributions of $\sim 20\%$ to overall
387 DFe are found in CESM runs along the northern part of west coast of India and the eastern BoB. Within Ganga-
388 Brahmaputra system, which is responsible for discharge of $\sim 11 \times 10^8 \text{ T yr}^{-1}$ of sediments, only 10% of sediments
389 is estimated to be transported longshore, with most of the sediments accumulating within the shelf and
390 subterranean canyon (Liu et al., 2009). Over the open ocean, sedimentary sources are most important within 10° -
391 15°S latitude where the South Equatorial Current is responsible for $\sim 50\%$ of DFe supply via advection from the
392 Indonesian shelf. During southwest monsoon, sedimentary contribution by the South Equatorial Current extends
393 farther westward ($\sim 70^\circ\text{E}$ longitude, Fig. S7c) compared to the northeast monsoon ($\sim 80^\circ\text{E}$ longitude, Fig. S6c).
394 Signatures of elevated Al due to sedimentary contribution is seen in ship-borne measurements (Grand et al., 2015;
395 Singh et al., 2020). In fact, such measurements have shown that the South Equatorial Current separates DFe-rich
396 oxygen-poor water of the northern IO from the DFe-poor oxygen-rich water of the southern tropical IO (Grand et
397 al., 2015).

398 River sources contribute negligibly to total DFe concentrations (Fig. 3d), except in the immediate vicinity of the
399 mouths of large river systems in the northeast BoB: the Ganges-Brahmaputra and the Irrawady-Sittang-Salween.
400 This is possibly because flocculation at the river mouth can quickly lead to near-complete losses of DFe compared
401 to other metals (Flegel et al., 1991; Sholkovitz, 1978). Hydrothermal vents also contribute negligibly to DFe
402 concentrations in the upper 100 m (Fig. 3e). The hydrothermal vents supplying DFe (often excess of 1.5 nM) in
403 the northern IO are located in the Central Indian Ridge and the Carlsberg Ridge (Chinni & Singh, 2022; Nishioka
404 et al., 2013; Vu & Sohrin, 2013), and largely influence DFe concentrations below 1000 m depths. The shallowest
405 hydrothermal plumes enriched with Fe are located between ~ 650 -900 m in the Gulf of Aden (Gamo et al., 2015),
406 overlapping with the depth range at which the Red Sea watermass spreads along the western IO (Beal et al., 2000).
407 Since this watermass occupies progressively deeper depths with distance, sliding underneath Persian Gulf waters,
408 surface DFe values are not impacted by these shallower vents. This is in concordance with simulations of
409 Tagliabue et al. (2010) where, following 500 years of model integration, hydrothermal vents increase globally
410 averaged DFe concentrations by only $\sim 3\%$ in the depth range of 0-100 m.

411 The average contribution of different sources of iron to the upper 100 m is summarized for different open ocean
412 regions over the northern IO in Fig. 3f. Annually averaged atmospheric deposition is clearly the most important
413 source of DFe throughout the northern IO. This source accounts for almost the entire supply of DFe over the
414 equatorial IO. The exception to the dominant role of atmospheric deposition is the southern tropical IO, where
415 sedimentary sources of iron contribute $\sim 40\%$ to the upper ocean iron budget. Overall, river contribution is
416 generally $\sim 1\%$, with slightly higher contributions in BoB and the southern tropical IO. Hydrothermal vents make
417 negligible contributions throughout the northern IO. Adding these four sources of DFe estimated from CESM
418 experiments does not yield the full 100% of the DFe source, possibly owing to non-linear effects associated with
419 iron removal processes as well as complexation by organic ligands.

420



421
 422
 423
 424
 425
 426
 427
 428
 429
 430

Figure 3: Contribution of different sources of DFe averaged over the year to the total DFe concentrations over the upper 100 m. Shading in (a) shows total DFe concentration with all sources included and shadings in (b-e) shows DFe concentrations arising from individual source. Contours in (b-e) show the percentage contribution of each source to total DFe concentrations. (f) Bar chart depicting source-specific DFe contribution (in %) over Bay of Bengal (BOB), Arabian Sea (AS), equatorial IO (EQIO), and the southern tropical IO (STIO). These regions are marked by the dashed boxes in (a). The thick black contour in (a) traces the 1000 m bathymetry.

431 3.3 Phytoplankton responses to multiple iron sources

432 In this section, the impact of different sources of DFe on phytoplankton growth is examined. Since river and
 433 hydrothermal sources make negligible contributions to the upper ocean iron concentrations, as shown above, these
 434 are not considered further.

435 3.3.1 Responses to atmospheric depositions

436 During the northeast and southwest monsoons, atmospheric DFe brings about increases in column-integrated
 437 chlorophyll concentrations over most of the northern IO (Figs. 4 a and c). The largest column-integrated positive
 438 response is seen in the western AS (west of ~65°E longitude) throughout the year, where atmospheric DFe
 439 accounts for more than ~20% of the column-integrated chlorophyll concentration and more than 50% of surface
 440 chlorophyll concentration (Fig. S8). This region comes under the influence of upwelling during the southwest
 441 monsoon and mixed layer deepening due to winter convection during the northeast monsoon, which can supply
 442 macronutrients required for phytoplankton growths (Madhuratap et al., 1996; Morrison et al., 1998). The other
 443 region displaying a strong positive response is the southern tropical IO during June-September, where atmospheric
 444 DFe contributes ~20% (~35%) of the column (surface) chlorophyll concentration. This is the time of the year
 445 when deep mixed layer leads to entrainment of nutrients into the surface layers (Košić et al., 2009; Lévy et al.,

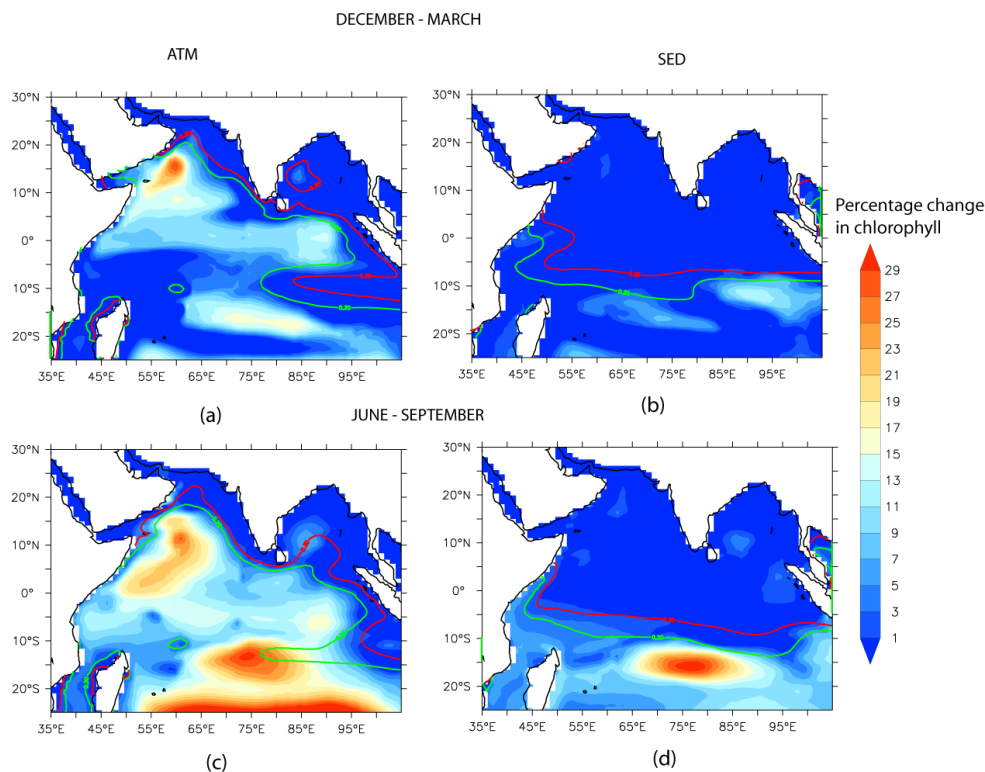


446 2007). In contrast, there are some regions, like the northern and western AS, the west coast of India and large
447 parts of the BoB and the eastern IO, which in spite of receiving high atmospheric DFe hardly experience any
448 chlorophyll response. These regions show <1% increase in column chlorophyll concentrations and generally
449 coincide with high sedimentary iron input. This is discussed further in Section 3.3.3.

450

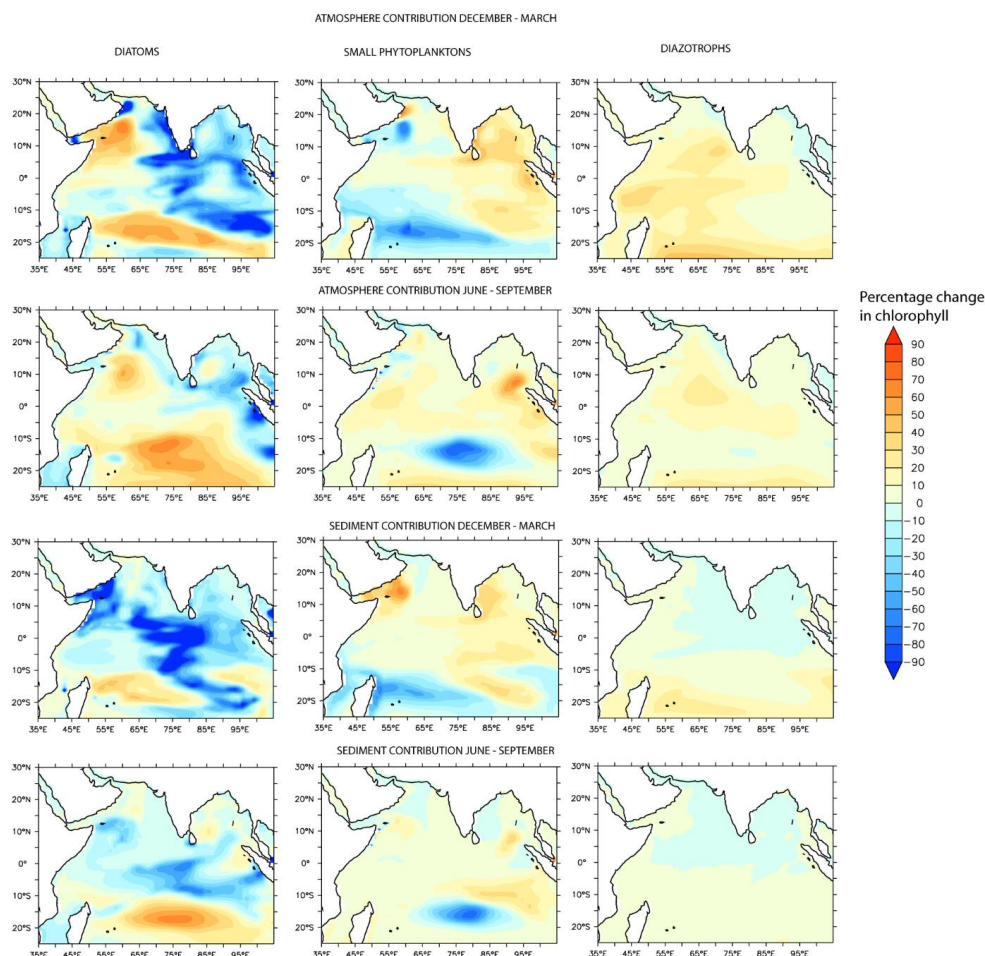
451 Species-wise decomposition shows that the increases in chlorophyll during both northeast and southwest
452 monsoons are driven by increases in diatoms and declines in small phytoplankton (Fig. 5). For example, over the
453 western AS and southern tropical IO, diatoms increase by at least 40% and small phytoplankton populations
454 decline by at least 50%. Diatoms outperforming other phytoplankton species has been previously witnessed in *in*
455 *situ* iron fertilization experiments (de Baar et al., 2005). This is due to the large cell size of diatoms enabling
456 higher cellular uptake of iron and also the ability of diatoms for luxury iron uptake, which enables them to
457 outcompete other species in a bloom (Sunda & Huntsman, 1995). An exception is the equatorial IO, where the
458 positive response of chlorophyll arises from growth of small phytoplankton. In general, this region has very low
459 levels of macronutrients and is dominated by picoplankton (Vidya et al., 2013). Those regions exhibiting <1%
460 increase in phytoplankton in response to atmospheric DFe, in contrast, are characterized by proliferation of small
461 phytoplankton and reductions of diatoms. Although diazotrophs show positive response to atmospheric DFe
462 addition throughout the region, this group constitutes only ~1% of total phytoplankton biomass. Such shifts in
463 phytoplankton community structure in response to DFe additions are also corroborated by *in situ* experiments
464 over the northern IO. For example, a nutrient addition experiment over the northern AS during northeast monsoon
465 period has shown that the maximum positive phytoplankton response takes place due to nitrate+DFe addition
466 (instead of only DFe addition), accompanied by around four-fold increases in coccolithophores, pennate and large
467 centric diatoms (Takeda et al., 1995). Ship-board iron addition experiments over the AS during the southwest
468 monsoon resulted in proliferation of visible colonies of haptophyte *Phaeocystis sp.* due to silicate-limitation
469 (Moffett et al., 2015). Over the eastern IO, where both macronutrients and micronutrients are low, nutrient spiking
470 with nitrogen, phosphorus, and iron resulted in increase of *Prochlorococcus*, *Synechococcus*, as well as Eukaryotes
471 (Twining et al., 2019).

472



473

474 **Figure 4: Percentage contribution of (a and c) atmospheric and (b and d) sedimentary sources of iron during (a and b)**
475 **the northeast monsoon and (c and d) the southwest monsoon to column-integrated (0-100 m depth) chlorophyll**
476 **concentrations. Green and red contours show background DFe concentrations of 0.2 nM and 0.3 nM respectively. For**
477 **the ATM (SED) case, background DFe is obtained from NATM (NSED) simulation.**
478



479

480 **Figure 5: Species-wise percentage contribution to column chlorophyll (0-100 m) response associated with atmospheric**
481 **and sedimentary sources of DFe.**

482

483

484

3.3.2 Responses to sedimentary sources of iron

485

As shown in Fig. 3, sedimentary sources supply less than ~20% of DFe north of ~10°S latitude, whereas between
10°-15°S latitude sedimentary iron can contribute to almost half the total DFe concentrations. Unlike atmospheric
sources, sedimentary supply of DFe is mostly confined to regions adjoining continental shelves and islands from
where they are introduced to the open ocean by seasonally varying currents. In general, sedimentary sources make
modest contribution to column productivity (<1% of chlorophyll anomalies) to the north of ~10°S latitude as
described above. This is because high dust deposition to the north of the intertropical convergence zone results in
high background DFe concentrations and controls productivity (see also Section 3.3.3). Sedimentary sources
trigger the strongest positive phytoplankton response over the southern tropical IO region during June-September,
where sedimentary DFe advected by the South Equatorial Current can facilitate more than 20% increase of the
upper 100 m chlorophyll concentrations and ~40% increase at the surface. As noted in Section 3.2, although

494



495 atmospheric deposition contributes nearly half of the total DFe addition to this region, the total iron deposition
496 here is low (<0.2 nM). The phytoplankton response over the southern tropical IO is dominated by an increase in
497 diatoms, which contribute to more than 60% of total phytoplankton biomass (Fig. 5). In contrast, over the regions
498 experiencing $<1\%$ chlorophyll increase, there is a shift from diatoms towards small phytoplankton species (Fig.
499 5). For example, there is more than 80% reduction in diatoms and 50% increase in small phytoplankton over the
500 western AS. Other current systems such as the poleward flowing Somali current, the eastward flowing Southwest
501 Monsoon Current and its southward extension along the west coast of Indonesia also transport sedimentary DFe
502 to the open ocean, but such advection supports only $\sim 5\%$ phytoplankton biomass.

503 3.3.3 Role of background nutrients in phytoplankton responses to external iron

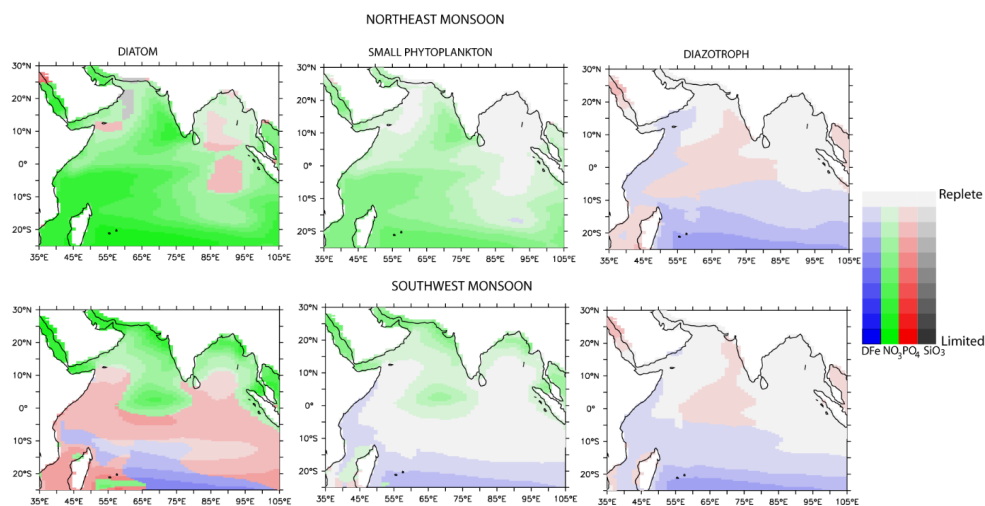
504

505 It emerges from the previous sections that there is heterogeneity in the phytoplankton response to atmospheric
506 and sedimentary sources of DFe. The regions of highest DFe input from a specific source are not always the
507 regions where strongest phytoplankton responses are evoked. What explains these differing patterns of
508 phytoplankton response? To examine this, patterns of nutrient limitations and iron supply from an external source
509 with respect to background DFe and nitrate (NO_3) concentrations are examined. In considering the phytoplankton
510 response to atmospheric sources (ATM case), background DFe is taken from the simulation without any
511 atmospheric source (NATM). Since river and hydrothermal sources make negligible contributions to DFe over
512 this domain, high levels of DFe in NATM mainly arise in regions where sedimentary sources are important.
513 Similarly, for estimating phytoplankton response to sedimentary sources (SED case), background DFe is taken
514 from simulation without any sedimentary source (NSED).

515 Generally, those regions experiencing greater than 1% increase in chlorophyll in response to atmospheric
516 (sedimentary) sources coincide with background DFe concentration <0.2 - 0.3 nM and high background NO_3 :DFe
517 ratio from the NATM (NSED) simulation. For example, in NATM simulation, iron serves as the dominant nutrient
518 that limits productivity over the entire northern IO, with diatoms experiencing stronger iron limitation compared
519 to other phytoplankton groups (Fig. S9). Iron limitation is particularly severe over central and southern AS,
520 equatorial IO and the southern tropical IO. In NSED case, there is a switch from nitrate limitation to the north of
521 the intertropical convergence zone to iron limitation to the south of the intertropical convergence zone (Fig. S10).
522 While iron stress is alleviated with addition of external DFe, there is a shift towards macronutrient, especially
523 nitrate, limitation (Fig. 6). South of $\sim 15^\circ\text{S}$ latitude continues to experience iron limitation during June-September
524 due to very low dust deposition. In contrast, regions where chlorophyll increase is $<1\%$ following DFe addition
525 are characterized by nitrate limitation in NATM/NSED simulations and external DFe cannot alleviate this primary
526 nutrient limitation. This is further illustrated in Fig. 7 where NO_3 :DFe ratio is plotted against background DFe
527 concentrations. Positive chlorophyll response is elicited in regions of lowest background DFe and highest
528 NO_3 :DFe ratio. Over the world oceans, a wide range of DFe:C ratio has been observed for diatoms, ranging from
529 4.3×10^{-5} for DFe-replete conditions to 2.0×10^{-6} for DFe-deplete conditions (de Baar et al., 2008). Assuming
530 C:N ratio of 117:16 (Anderson and Sarmiento, 1994), range of N:DFe ratios obtained are ~ 3000 and ~ 68000 ,
531 respectively, for DFe-replete and DFe-deplete conditions. Similarly, by considering iron limitation taking place
532 for DFe:C ratio of 1×10^{-5} for open ocean species based on laboratory experiments (Sunda & Huntsman, 1995)
533 and C:N ratio of 106:16, Measures and Vink (1999) have estimated that iron limitation over the AS takes place at
534 NO_3 :DFe ratio greater than ~ 15000 . In CEM simulations $>1\%$ increase in chlorophyll takes place when initial

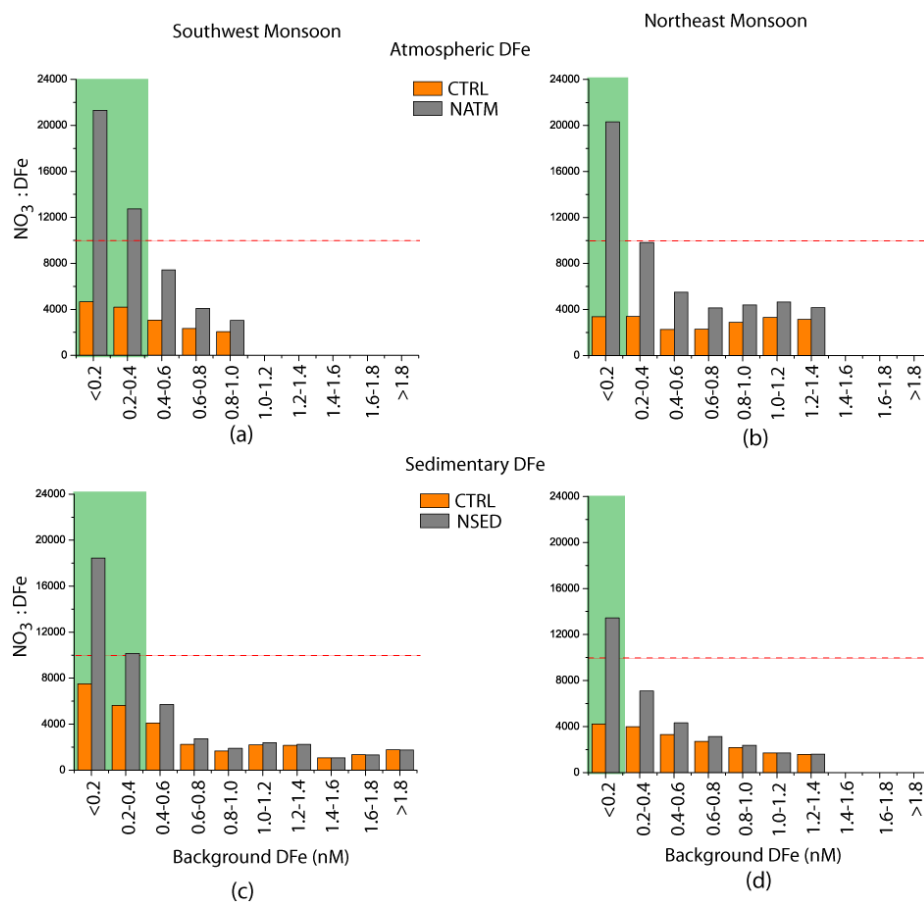


535 NO_3 :DFe ratio is more than 10,000 corresponding to Fe-limitation scenario (Fig. 7). With the addition of DFe
536 from atmospheric or sedimentary sources, the NO_3 :DFe ratio reduces to even less than ~4000 in some cases,
537 thereby leading to N-limitation. Previously, iron addition experiments in AS during the southwest monsoon have
538 shown that the positive chlorophyll response depends on initial nitrate concentrations, with this response
539 increasing in magnitude with higher initial nitrate concentrations (Moffett et al., 2015). In summary, the initial
540 NO_3 :DFe ratio sets the ultimate limit to the magnitude and distribution of phytoplankton response following
541 external DFe additions.
542



543
544
545
546
547

Figure 6: Patterns of surface nutrient limitations for different phytoplankton functional types from CTRL simulation. Green: nitrate; blue: iron; red: phosphate; grey: silicate limitations.



548

549 **Figure 7: Relation between background nutrients and phytoplankton response for atmospheric (a and b) and**
 550 **sedimentary (c and d) sources of DFe during (a and c) southwest monsoon and (b and d) northeast monsoon. The**
 551 **horizontal axis shows background DFe concentrations. The orange columns show NO₃:DFe ratio for CTRL case and**
 552 **grey columns show NO₃:DFe ratio for (a-b) NATM and (c-d) NSED cases. The red dashed lines show the location where**
 553 **NO₃:DFe ratio is 10,000: below this value N-limitation prevails in CESM. Green shades highlight the regions where**
 554 **>1% increase in chlorophyll following DFe addition from a specific source is induced.**
 555

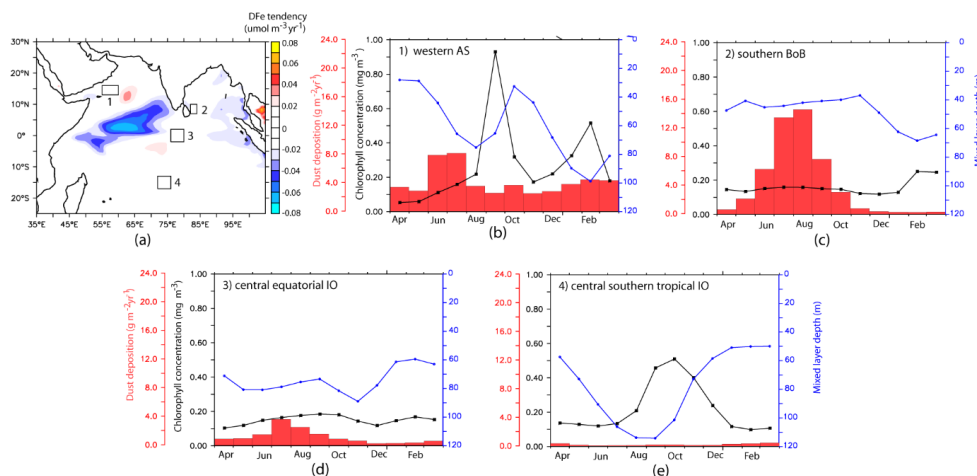
556 To sum up, atmospheric deposition is the most important source of DFe to the upper 100 m over the entire northern
 557 IO, followed by sedimentary sources. While atmospheric DFe is deposited over wide areas of the open ocean,
 558 sedimentary DFe fluxes arise only from continental shelves and are transported to open oceans through advection
 559 by currents. River and hydrothermal sources make negligible contributions to the total iron budget in the upper
 560 100 m. The primary response to atmospheric DFe is an increase in column-integrated phytoplankton biomass over
 561 most of the northern IO. In contrast, sedimentary source of iron is responsible for increases in column-integrated
 562 phytoplankton biomass mainly to the south of the intertropical convergence zone, where dust depositions are low.
 563 In general, significant positive responses of phytoplankton to addition of DFe are simulated only where low levels
 564 of background DFe concentrations and high values of background NO₃:DFe ratio are present. Otherwise, nitrate
 565 becomes the limiting nutrient once DFe is added. The simulations also show that positive chlorophyll response



566 to addition of DFe generally involves proliferation of diatoms, except over the equatorial IO where small
 567 phytoplankton increase is seen.

568
 569 **3.4 Iron budgets across different bio-physical regimes**

570 This section explores the main processes controlling DFe budget with respect to the role of atmospheric and
 571 sedimentary sources over different bio-physical regimes of the northern IO: (1) the western AS, (2) the southern
 572 BoB, (3) the central equatorial IO and (4) the central southern tropical IO. These regions encompass a wide range
 573 of productivity, with the first region being highly productive with OC-CCI chlorophyll exceeding 1.5 mg m^{-3} . The
 574 southern BoB and central southern tropical IO are moderately productive. Lastly, the central equatorial IO is
 575 oligotrophic with surface chlorophyll concentration being $\sim 0.1 \text{ mg m}^{-3}$. The locations of these regions along with
 576 CESM simulated seasonal cycles of mixed layer depths, chlorophyll and dust depositions are shown in Fig. 8.



577
 578 **Figure 8: (a) Net DFe tendency averaged over the upper 100 m for the study period. The boxes indicate the regions**
 579 **chosen for further studying DFe budget in Section 3.4. (b-e) Seasonal cycle of dust deposition (red columns), mixed**
 580 **layer depth (blue curves) and chlorophyll concentrations (black curves) from CESM-CTRL case for the four regions**
 581 **marked in (a).**

582

583 The net dissolved iron tendency ($TEND_{DFe}$) is calculated as:

584
$$TEND_{DFe} = EXT + ADV + MIX + BIO \quad (1)$$

585 where the source terms on the right describe dust/sediments/rivers/vents (EXT), horizontal and vertical advection
 586 (ADV), horizontal and vertical mixing (MIX) and biological sources/sinks (BIO). Advection includes explicitly
 587 resolved velocity as well as an additional “bolus” velocity from parameterization of mesoscale eddies (Gent &
 588 McWilliams, 1990). Vertical mixing includes a tracer gradient dependent term for cross-isopycnal mixing and a
 589 non-local mixing term, which accounts for mixing due to convective and shear instabilities (Large et al., 1994).
 590 Lateral mixing involves parameterization of mesoscale eddy-induced horizontal diffusion along isopycnal
 591 surfaces (Redi, 1982). The BIO term includes DFe losses due to biological iron uptake and scavenging, recycling



592 of iron back to the pool via remineralization, and iron released from phytoplankton and zooplankton losses and
593 grazing.

594 3.4.1 Western Arabian Sea

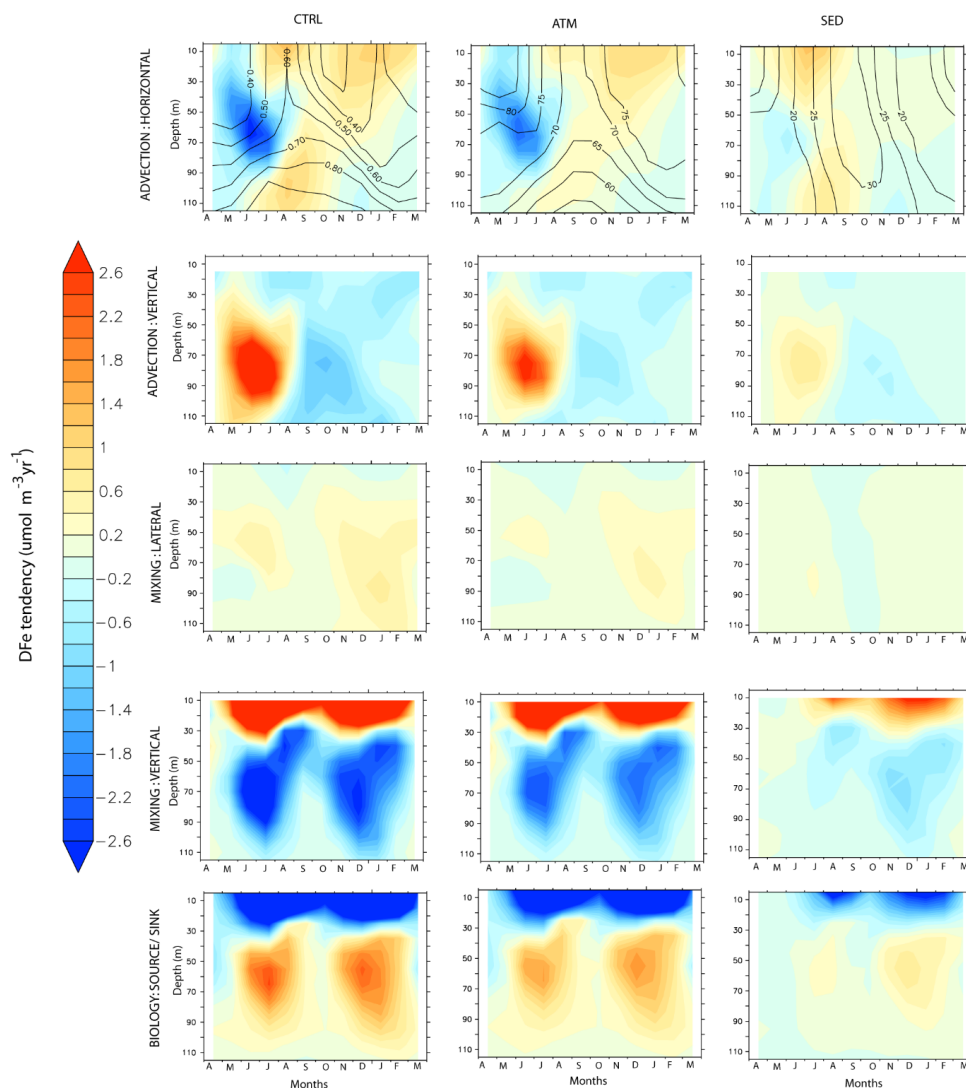
595 The western AS, off Oman and Yemen coastlines (considered here as 13°-16°N and 55°-60°E), is the most
596 productive region in the northern IO. Primary productivity in the western AS is highest during southwest monsoon
597 (Fig. 8b), during which alongshore southwesterly winds lead to upwelling and bring subsurface nutrients from
598 depths of ~150-200 m (Morrison et al., 1998). Some of this upwelled water advects eastwards, transporting
599 nutrients that enhance productivity in the central AS (Prasanna Kumar et al., 2001). The region also experiences
600 a secondary bloom during northeast monsoon due to winter convection that deepens the mixed layer. Integrated
601 over depths of the euphotic zone, average primary productivity over the western AS during mid and late southwest
602 monsoon is estimated at $135 \pm 10 \text{ mmol C m}^{-2} \text{ d}^{-1}$ and $110 \pm 11 \text{ mmol C m}^{-2} \text{ d}^{-1}$ respectively (Barber et al., 2001). In
603 comparison, primary productivity over the western AS during mid and late northeast monsoon is $137 \pm 13 \text{ mmol}$
604 $\text{C m}^{-2} \text{ d}^{-1}$ and $88 \pm 4 \text{ mmol C m}^{-2} \text{ d}^{-1}$ (Barber et al., 2001). Although this region encounters high dust deposition
605 (Haake et al., 1993; Mahowald et al., 2009), *in situ* measurements have hypothesized possible iron limitation
606 during late southwest monsoon because upwelled water is drawn from above the iron-rich sub-oxic zone (Naqvi
607 et al., 2010).

608 The largest peak in dust deposition is during southwest monsoon, followed by a second peak during northeast
609 monsoon (Fig. 8b). Accordingly, the upper ocean DFe concentration is highest during southwest monsoon and is
610 dominated by atmospheric sources (Fig. 9). Sedimentary contribution, although much lower, peaks during late
611 southwest monsoon and fall intermonsoon months. Throughout the year DFe concentration increases with depth,
612 thus pointing to consumption by phytoplankton at the surface. Vertical advection and vertical mixing are the most
613 important physical mechanisms governing DFe supply within this region during southwest monsoon (Fig. 9).
614 These processes begin to strengthen from May onwards to reach their peak during June-July and decrease
615 thereafter. Decomposing DFe advection tendency into tendencies arising from gradients in tracer distribution
616 ($D\text{Fe}'$) and velocity convergence (U') respectively, it is seen that vertical advection of DFe arises from $D\text{Fe}'$ and
617 U' in equal magnitude. However, the former process is dominant in June and the latter process dominates during
618 July (Fig. S11). The maximum vertical advection of DFe is centered around 80 m depth and progressively reduces
619 at shallower depths, as the vertical velocity reduces towards the surface. Vertical mixing prevailing in the upper
620 40 m brings this vertically advected DFe from subsurface to the surface. Furthermore, horizontal advection plays
621 an important role in redistributing this DFe supplied by vertical processes, with contributions from horizontal U'
622 being at least twice as large as $D\text{Fe}'$. During spring and early southwest monsoon, northeastward horizontal
623 advection removes atmospheric deposited DFe throughout the upper 100 m, while aiding the supply of
624 sedimentary DFe from Somalia and Omani continental shelves to the western AS. Later in the year as the
625 southwest monsoon current circulation is established, and meridional currents along the western AS become
626 stronger, its effect is first evident in the south along the Somali coast and progresses northward with time. The
627 result is convergence of both atmospheric and sedimentary DFe in the western AS during July-September. During
628 northeast monsoon, vertical mixing driven by winter convection, with the mixed layer deepening to 100 m, is the
629 most important means of DFe supply, from both atmospheric and sedimentary sources, into the surface layer.



630 Additionally, horizontal advection by westward currents transports DFe from atmospheric deposition in the central
631 AS into the western AS.

632 Removal of DFe from the water column is mainly through biological uptake in the upper 40 m. Uptake of DFe by
633 small phytoplankton dominate biological uptake throughout the year, except during September-October when
634 diatoms uptake of DFe becomes significant (not shown). This signature of diatoms is also observed in opal fluxes
635 measured by sedimentary traps deployed near the western AS and has been attributed to lowering of zooplankton
636 grazing pressures during late southwest monsoon (Smith, 2001) as well as to silicate limitation of diatoms in
637 initially upwelled waters (Haake et al., 1993). In the subsurface layer, remineralization of sinking fluxes of
638 particulate iron peaking at ~50 m replenishes the DFe pool during the latter part of the productive months (Fig.
639 S15a). Iron so released is made available to the surface layer via mixing or advection, thereby playing an important
640 role in maintaining surface DFe pool. Some of the remineralized DFe is further removed by scavenging, which
641 peaks at ~80 m during the productive months due to large fluxes of sinking particulate organic carbon, biogenic
642 silica, calcium carbonate and dust (Fig. S15a). Atmospheric deposition dominates biological source/sink of DFe
643 throughout the year, while sedimentary DFe is more important for biology during northeast monsoon months.



644
 645 **Figure 9:** Evolution of the various terms of DFe budget, expressed as $\mu\text{mol m}^{-3} \text{yr}^{-1}$, by month and depth over the
 646 western Arabian Sea. Left panels: CTRL, Middle panels: ATM and, Right panels: SED case. The contours in the upper
 647 panel for CTRL show evolution of DFe concentrations (nM), while the contours in the upper panels for ATM and SED
 648 cases show the percentage contribution of each of these cases to total DFe concentrations in CTRL case.

649

650 3.4.2 Southern Bay of Bengal

651 The region corresponding to the southern BoB (7° - 10°N and 82° - 84°E) is located to the east of Sri Lanka.
 652 Compared to the rest of the BoB, freshwater flux from South Asian rivers reduces markedly in this region due to
 653 advection of high salinity water from AS by the eastward flowing Southwest Monsoon Current (see Fig. 1h) as
 654 well as upward pumping of saltier water by thermocline doming during the southwest monsoon season
 655 (Vinayachandran et al., 2013). This leads to stronger biophysical coupling in the southern BoB, compared to the
 656 rest of the bay, through erosion of the upper stable layer of freshwater capping. During southwest monsoon, the



657 Southwest Monsoon Current advects nutrients and chlorophyll from the upwelling regions along the southern tip
658 of India and Sri Lanka into the southern BoB (Vinayachandran et al., 2004). Over the open southern BoB, to the
659 east of Sri Lanka, cyclonic wind stress curl drives open ocean upwelling leading to shoaling of the thermocline
660 that forms the Sri Lankan dome. This results in surface chlorophyll concentration between 0.3-0.7 mg m⁻³ and
661 strong subsurface chlorophyll maxima between 20-50 m where chlorophyll concentration can exceed 1 mg m⁻³
662 (Thushara et al., 2019). A much lower magnitude of surface chlorophyll concentration (~0.18 mg m⁻³, Fig. 8c)
663 and subsurface chlorophyll maxima (~0.2 mg m⁻³) at 40-60 m depth is simulated by CESM. During the northeast
664 monsoon, CESM simulates a second bloom over this region associated with winter cooling and mixed layer
665 deepening to ~60 m (Fig. 8c). This bloom has slightly higher magnitude, peaking at ~0.25 mg m⁻³, compared to
666 the southwest monsoon bloom. Surface chlorophyll data from OC-CCI also reveals the presence of northeast
667 monsoon blooms (peak at ~0.25 mg m⁻³), which during some years are of higher magnitude than southwest
668 monsoon blooms. Argo data in this region also show signatures of mixed layer deepening during winter (not
669 shown).

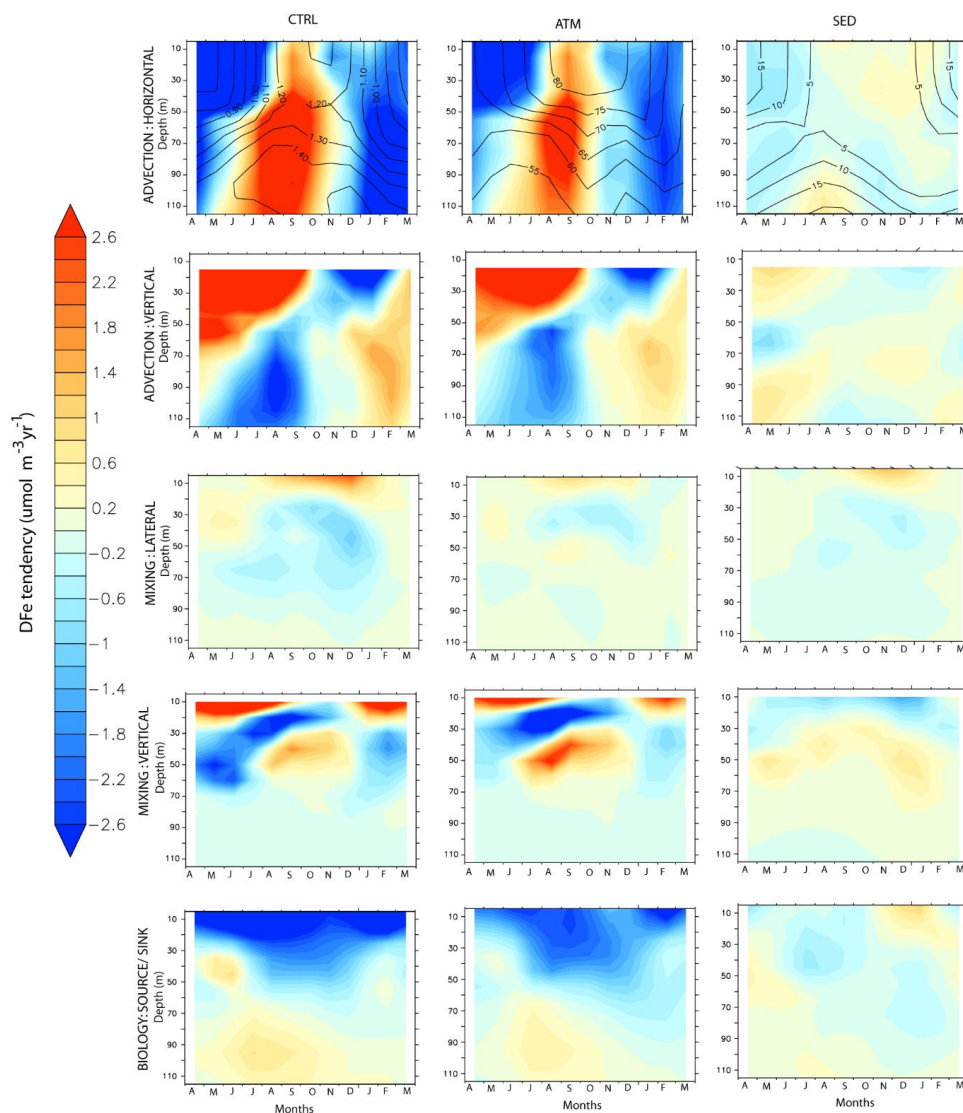
670 Overall, the highest DFe over this region is encountered during the late southwest monsoon and is dominated by
671 atmospheric deposition (Fig. 10). Vertical advection is the most important process supplying DFe to the surface
672 layers during spring and southwest monsoon months (Fig. 10). This is aided by a positive wind stress curl
673 established over the region from March onwards. While vertical velocity is positive during the southwest monsoon
674 over the entire depth considered, DFe supply by vertical advection is positive only for depths less than 50 m (Fig.
675 S12). This is because the magnitude of upward velocity gradually reduces with depth, resulting in positive values
676 of U' upwards from 40 m depths. (Fig. S12). With the arrival of westward propagating Rossby waves to the
677 western boundary of the BoB during October, upwelling favorable vertical motion collapses (Webber et al., 2018).

678 With respect to horizontal advection, it is seen that the magnitude and sign of convergence by the meridional
679 component of the current mainly controls DFe supply over the southern BoB. This arises from the southward
680 flowing current to the western flank of the Sri Lankan dome that supplies atmospheric DFe to this region. This
681 DFe supplied by the southwards current, as well as DFe derived from upwelling, is removed by the energetic
682 eastward currents during late spring to early fall intermonsoon months. During the rest of the year, the westward
683 flowing currents supplies some sedimentary DFe from the Andaman Sea to the southern BoB. However, the much
684 larger magnitude of dust deposition in the north-western BoB leads to overall negative tracer gradients and, thus,
685 dilution of DFe by horizontal advection. The most important DFe supply mechanism during northeast monsoon
686 is enhanced vertical mixing in the upper 20 m associated with deepening of mixed layer. Additionally,
687 downwelling due to weakly negative wind stress curl during this time of the year removes DFe from the surface
688 and favors its accumulation in the subsurface ocean. Lateral mixing complements DFe supply to the upper 20 m
689 during fall and early northeast monsoon, especially from sedimentary sources.

690 Biological uptake removes DFe throughout the year from the upper 40 m especially during the southwest and
691 northeast monsoon blooms (Fig. 10). DFe uptake in the upper 40 m is dominated by small phytoplankton during
692 most of the year, except during northeast monsoon (not shown). Diatom DFe uptake, on the other hand, dominates
693 the deep chlorophyll maxima present between 40-70 m throughout the year as well as within the surface layer
694 during northeast monsoon months. Several studies have pointed to substantial nutrient uptake by diatoms in the
695 central, coastal, and northern BoB due to riverine supply of silicates (Madhu et al., 2006; Madhupratap et al.,



696 2003). Remineralization of DFe as well as DFe release from grazing and mortality of phytoplankton and
 697 zooplankton have a primary peak between 50 m-80 m during July-August and secondary peak during February-
 698 March. On the contrary, scavenging removes DFe, with its effect peaking during July-August during blooms (Fig.
 699 S15b).



700

701 **Figure 10: Same as Figure 9, except over the southern Bay of Bengal.**

702

703 **3.4.3 Central Equatorial IO**

704 With chlorophyll concentrations around 0.1 mg m^{-3} for most part of the year, the central equatorial IO ($2^{\circ}\text{S}-2^{\circ}\text{N}$
 705 and $76^{\circ}-80^{\circ}\text{E}$) is the least productive of all the regions considered (Fig. 8d). Unlike its counterparts in the Pacific

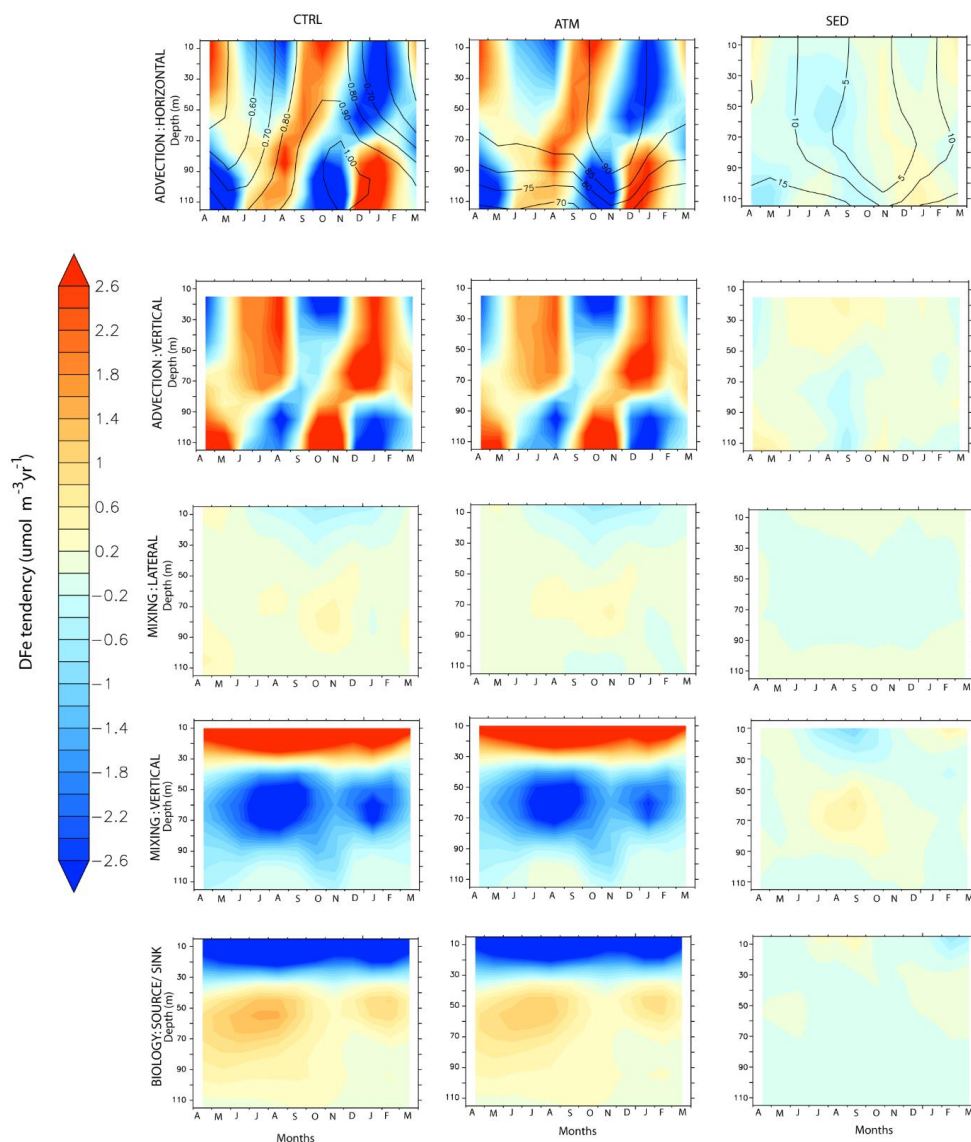


706 and the Atlantic Oceans, the equatorial IO experiences only transient upwelling due to changes in wind direction
707 associated with migration of the intertropical convergence zone. This also leads to surface currents reversing their
708 direction four times a year. Thus, the region experiences westward surface currents of weak magnitude during the
709 southwest and northeast monsoon months and much stronger eastwards current during the spring and fall
710 intermonsoon months (Han et al., 1999). These narrow eastwards surface currents during the intermonsoon
711 months, known as Wyrki jets, are in response to westerly winds (Wyrki, 1973). The biogeochemical
712 characteristics of the region have only been recently explored with the help of satellite and *in situ* data (e.g.,
713 Prasanna Kumar et al., 2012; Strutton et al., 2015). Deepening of the surface layer associated with the eastward
714 transport of water during the intermonsoon months lowers productivity (Prasanna Kumar et al., 2012).
715 Chlorophyll concentrations, although much lower compared to the rest of the IO, peaks during October-December
716 possibly due to wind stirring or shear instability at the base of the eastward moving Wyrki Jet (Strutton et al.,
717 2015). Additionally, *in situ* measurements in the central equatorial IO have revealed deep chlorophyll maxima
718 located ~60 m depth contributing to more than 30% of the total chlorophyll biomass (Vidya et al., 2013). The
719 peak ocean DFe concentration is encountered during August-November. Overall, comparison between CTRL,
720 ATM and SED cases show that atmospheric deposition, peaking during July (Fig. 8d), dominates DFe contribution
721 to the central equatorial IO, whereas sedimentary DFe plays a distant secondary role (Fig. 11).

722 Horizontal advection is the most important process of DFe supply within the mixed layer during March-May and
723 September-November (Fig. 11). During the intervening months, vertical advection plays the predominant role in
724 DFe supply. Decomposing the horizontal advection further into DFe' and U' reveals that the meridional velocity
725 convergence is the main contributor to the central equatorial IO DFe budget during March-May and September-
726 November (Fig. S13). This originates from the westerly wind directing equatorward Ekman flow in both the
727 hemispheres, which leads to convergence and drives eastward propagating downwelling Kelvin wave (McPhaden
728 et al., 2015). Averaged over the upper 100 m, zonal velocity convergence, although somewhat of lower magnitude,
729 opposes meridional velocity convergence throughout the year. When the Wyrki jet weakens, upwelling induced
730 by easterly wind drives upward vertical supply of DFe, whereas there is downward vertical removal of DFe during
731 the intervening periods. This alternating between upwelling and downwelling control on DFe has an upward phase
732 propagation. An important feature of the central equatorial IO, in contrast to other equatorial regions, is the
733 presence of transient Equatorial Undercurrent between 60 m-200 m depth with core generally centered on the
734 depth of the 20°C isotherm (Chen et al., 2015). The Equatorial Undercurrent appears most strongly during winter-
735 spring months and with much weaker magnitude during summer-fall months (Chen et al., 2015; Schott &
736 McCreary, 2001). CESM simulation reveals the signature of the upper part of the Equatorial Undercurrent in
737 influencing DFe budget. This is characterized by the zonal velocity underneath the mixed layer (~80 m depth)
738 showing strong eastward transport during January-April and a much weaker eastward transport during September-
739 November. The horizontal convergence of DFe is prominent during the developing phase of the Equatorial
740 Undercurrent (December-February and June-August), probably, associated with progressive eastward extension
741 and strengthening of Equatorial Undercurrent from the western IO. These periods of horizontal DFe convergence
742 are interspersed with vertical DFe convergence. Superimposed on advection, vertical mixing plays an important
743 role in bringing subsurface DFe to the surface levels in the upper 30 m, peaking during July-August.



744 Biological removal of DFe, almost entirely by small phytoplankton, is conspicuous in the upper 40 m and peaks
745 during September. This is in line with sediment trap studies over the central equatorial IO where peak biogenic
746 fluxes are detected during the southwest and fall intermonsoon months and are dominated by foraminifera
747 carbonate (Ramaswamy and Gaye, 2006). Furthermore, *in situ* water samples have shown that picoplankton,
748 having size less than 10 μm , consists of more than 90% of the phytoplankton biomass in central equatorial IO
749 (Vidya et al., 2013). The period of peak biogenic flux is also characterized by peak in DFe removal by scavenging
750 and remineralization of DFe released from mortality and grazing at deeper layers (Fig. S15c). A secondary
751 increase in biological removal of DFe is noticed during January-March associated with a secondary peak in
752 chlorophyll, although its impact is not evident in sediment trap biogenic flux data (Vidya et al., 2013). This might
753 arise from remineralization of DFe being almost twice the magnitude of scavenging losses during this time of the
754 year.



755

756 **Figure 11: Same as Figure 9, except over the central equatorial Indian Ocean.**

757

758 **3.4.4 Central Southern Tropical IO**

759 The central southern tropical IO (13°-17°S and 72°-76°E) is located in the transition zone between DFe-poor region
 760 of the subtropical IO gyre and DFe-enriched northern IO. Of all the regions considered, this receives the lowest
 761 atmospheric DFe (Fig. 8e), resulting in DFe limitation of phytoplankton growth particularly during the boreal
 762 summer (Fig. 6). Steady southeasterly winds, prevailing throughout the year, transport dust from Australian
 763 sources into this region. Peak in dust deposition is during austral spring and summer associated with strong source

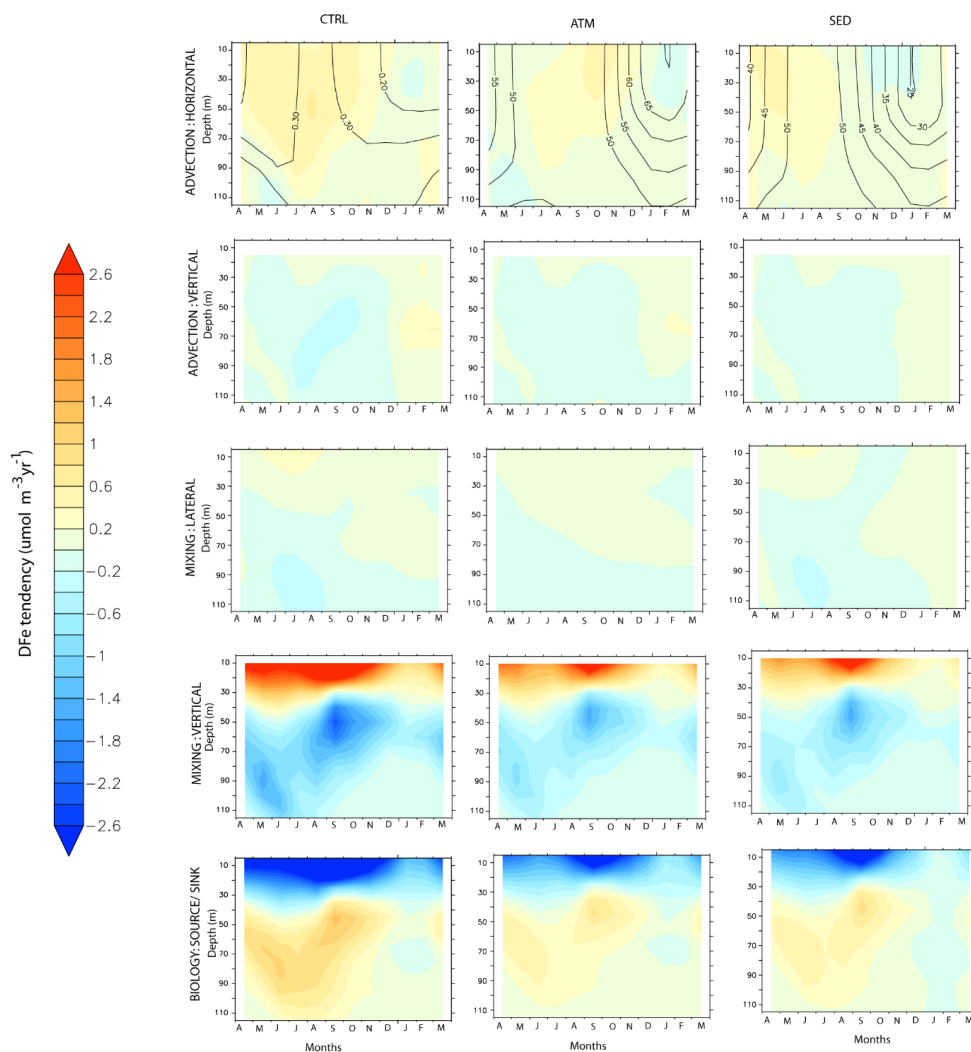


764 activity (Kok et al., 2021; Yang et al., 2021). A secondary peak in dust deposition during austral winter is possibly
765 associated with enhanced transport. Northern part of the central southern tropical IO lies on the Seychelles-Chagos
766 thermocline ridge, which is characterized by doming up of the thermocline due to negative wind stress curl
767 resulting in Ekman divergence (Vialard et al., 2009). The thermocline progressively deepens towards the sub-
768 tropical southern IO gyre to the south as wind stress curl changes sign to positive. The westward flowing South
769 Equatorial Current brings low salinity water and nutrients from the Indonesian region. Satellite observed enhanced
770 chlorophyll concentration during the boreal (austral) summer (winter) months have been attributed to vertical
771 diffusion (Košič et al., 2009; Lévy et al., 2007). Additionally, westward propagating upwelling/downwelling
772 Rossby waves arrive in this region following La Nina/El Nino event and play a key role in modulating sea surface
773 height and the depth of thermocline (Masumoto & Meyers, 1998; Périgaud & Delecluse, 1992). This perturbs the
774 depth of nitracline, which has significant impact on column productivity (Kawamiya & Oschlies, 2001).

775 Both ATM and SED sources are important in this region for DFe supply, with the SED (ATM) source having
776 higher contribution during austral winter (summer) months (Fig. 12). Analysis of CESM-simulated DFe budget
777 reveals that vertical mixing in the upper 30 m is the most important process of DFe supply, which peaks during
778 September. This is the time of the year when CESM records the lowest sea surface temperature resulting in mixed
779 layer deepening. Such winter mixing leads to erosion of vertical gradient in DFe observed during the rest of the
780 year in the upper 120 m. Horizontal advection is the next most important supplier of DFe in this region. The
781 westward flowing South Equatorial Current is strongest during austral winter and during winter-to-summer
782 transition months. This results in meridional velocity convergence and zonal velocity divergence resulting in a
783 quasi-balance between DFe supply and removal (Fig. S14). Overall, horizontal advection leads to predominantly
784 sedimentary DFe convergence during March-June and predominantly atmospheric DFe convergence during
785 September-November.

786 The wind stress curl is mostly negative, that is upwelling favorable, throughout the year. Between April-October
787 (austral winter), when winter convection-driven blooms are prominent, wind stress curl becomes weakly negative
788 to slightly positive. Following this, during January-March, the wind stress curl becomes strongly negative
789 resulting in upward velocity and favors vertical advection of both atmospheric and sedimentary DFe in equal
790 magnitude. While vertical U' is responsible for supplying DFe in the upper 50 m, vertical DFe' is important at
791 deeper depths (Fig. S14).

792 The biological sink of DFe peaks during the month of maximum vertical mixing, that is, during September.
793 During this time, uptake of DFe is dominated by diatoms, which accounts for more than 80% of the total DFe
794 uptake. Small phytoplankton dominate the rest of the year. Scavenging removal of DFe and remineralization peaks
795 one month later during October between 50-90 m depth range (Fig. S15d). Overall, the central southern tropical
796 IO is the only region where atmospheric deposition and sedimentary sources of iron are equally important in
797 driving the DFe budget.



798

799 **Figure 12: Same as Figure 9, except over the central southern tropical Indian Ocean.**

800

801 **4 Conclusions**

802

803 Using the ocean component of the Earth system model CESM version 2.1, this study elucidates the impacts of
804 various sources of DFe on upper ocean productivity, nutrient limitations and DFe budgets over the northern IO.
805 The iron cycle in CESM represents the complex interplay between several processes including DFe supply,
806 removal by scavenging and biological uptake, DFe remineralization, and organic ligand complexation. The major
807 sources of DFe for this region are included in this model: atmospheric deposition, sediments, hydrothermal vents,
808 and rivers. Although there are model biases in representing physical and biogeochemical variables, the overall
809 patterns of spatial and temporal variation of DFe are simulated reasonably well in CESM.



810 The study finds that atmospheric deposition is the most important source of DFe to the northern IO. Atmospheric
811 deposition contributes well over 50% of the total DFe concentration and more than 10% (35%) to upper 100 m
812 (surface level) chlorophyll concentrations, especially over the AS, equatorial IO, and southern tropical IO.
813 Sedimentary sources become important along continental shelves, where they can contribute to more than 20% of
814 total DFe. The sedimentary source has the largest impact in fueling phytoplankton blooms over the southern
815 tropical IO during June-September. In contrast, hydrothermal and river sources have negligible impacts on upper
816 ocean DFe pools in this region. Almost all regions that experience significant positive chlorophyll responses to
817 atmospheric as well as sedimentary sources of DFe show a preponderance of diatoms over other phytoplankton
818 groups. The increases in phytoplankton following external DFe addition are evoked in regions with low
819 background DFe levels (<0.3 nM) and high initial NO_3 :DFe, indicating the importance of high levels of
820 macronutrients. Following, external DFe addition, a shift to nitrate limitation of phytoplankton is observed.

821 Analysis of DFe budget across different biophysical regimes in the northern IO shows that this budget is generally
822 dominated by atmospheric deposition, with sedimentary sources of DFe being a distant second contributor. The
823 exception to this occurs over the southern tropical IO region, where both atmospheric and sedimentary sources
824 become equally important. In all the regions considered, vertical mixing is the most important physical mechanism
825 through which DFe is supplied, and furthermore this mechanism is active almost throughout the year. In contrast,
826 the importance of horizontal and vertical advection is highly seasonal. DFe uptake by small phytoplankton in the
827 upper ocean is the most important route through which DFe removal takes place, except in the productive waters
828 where diatoms also participate in the removal process. At subsurface levels, competition between the removal of
829 DFe by scavenging and its remineralization determines the DFe pool available to the surface ocean via these
830 aforementioned physical processes.

831 Of all DFe sources, atmospheric deposition is most likely vulnerable to future global warming, and changes to it
832 will perhaps exert strong influence on upper ocean productivity and nutrient limitation. This study thus provides
833 foundations to explore how future scenarios of atmospheric deposition can impact biogeochemistry over the
834 northern IO.

835

836 **Code and data availability**

837 Climatology of ocean temperature, salinity and nutrients are from World Ocean Atlas 2018 available at
838 <https://www.ncei.noaa.gov/access/world-ocean-atlas-2018/>. Monthly surface chlorophyll data from OC-CCI is
839 obtained from <https://www.oceancolour.org/>. Monthly climatology of ocean mixed layer depth based on Holte et
840 al. (2017) is downloaded from <http://mixedlayer.ucsd.edu/>. Surface ocean current data from OSCAR can be
841 downloaded from: [https://podaac.jpl.nasa.gov/dataset/OSCAR_L4_OC_third-](https://podaac.jpl.nasa.gov/dataset/OSCAR_L4_OC_third-deg?ids=Keywords:Keywords:Projects&values=Oceans::Solid%20Earth::OSCAR&provider=PODAAC)
842 [deg?ids=Keywords:Keywords:Projects&values=Oceans::Solid%20Earth::OSCAR&provider=PODAAC](https://podaac.jpl.nasa.gov/dataset/OSCAR_L4_OC_third-deg?ids=Keywords:Keywords:Projects&values=Oceans::Solid%20Earth::OSCAR&provider=PODAAC).

843 Dissolved iron from GEOTRACES Intermediate Data Product 2021 is available at
844 <https://www.geotraces.org/geotraces-intermediate-data-product-2021/>. Additionally, dissolved iron profile data
845 are also obtained from Tagliabue et al. (2012) available at <https://www.bodc.ac.uk/geotraces/data/historical/>. The
846 code for CESM2.1 can be downloaded from https://www.cesm.ucar.edu/models/cesm2/release_download.html
847 (last access: 01 December 2020).



848 **Author contributions**

849 PB conceived the study, carried out model simulations, analysed the data and wrote the manuscript.

850 **Competing interests**

851 The author declares that there is no conflict of interest.

852 **Acknowledgments**

853 PB acknowledges the computational facilities provided by Supercomputer Education and Research Centre
854 (SERC) at the Indian Institute of Science for carrying out CESM simulations.

855 **Financial support**

856 The author is supported by Department of Science and Technology INSPIRE Faculty scheme
857 (DST/INSPIRE/04/2018/002625).

858 **References**

859 Anderson, L. and Sarmiento, J.: Redfield ratios of remineralization determined by nutrient data analysis, *Global*
860 *Biogeochem. Cy.*, 8, 65–80, <https://doi.org/10.1029/93GB03318>, 1994.

861 Armstrong, R. A., Lee, C., Hedges, J. I., Honjo, S., and Wakeham, S.: A new, mechanistic model for organic
862 carbon fluxes in the ocean: based on the quantitative association of POC with ballast minerals, *Deep-Sea Res.*,
863 49, 219–236, 2002.

864 Banerjee, P. and Kumar, S. P.: Dust-induced episodic phytoplankton blooms in the Arabian Sea during winter
865 monsoon, *J. Geophys. Res.-Oceans*, 119, 7123–7138,
866 <https://doi.org/10.1002/2014JC010304>, 2014.

867 Banerjee, P., Sathesh, S. K., Moorthy, K. K., Nanjundiah, R. S., and Nair, V. S.: Long-range transport of mineral
868 dust to the northeast Indian Ocean: Regional versus remote sources and the implications, *J. Clim.*, 32, 1525–1549,
869 <https://doi.org/10.1175/JCLI-D-18-0403.1>, 2019.

870 Barber, R. T., Marra, J., Bidigare, R. C., Codispoti, L. A., Halpern, D., Johnson, Z., Latasa, M., Goericke, R., and
871 Smith, S. L.: Primary productivity and its regulation in the Arabian Sea during 1995, *Deep-Sea. Res. Pt. II*, 48,
872 1127–1172, [https://doi.org/10.1016/S0967-0645\(00\)00134-X](https://doi.org/10.1016/S0967-0645(00)00134-X), 2001.

873 Beal, L. M., Field, A., and Gordon, A. L.: Spreading of Red Sea overflow waters in the Indian Ocean, *J. Geophys.*
874 *Res.*, 105, 8549–8564, <https://doi.org/10.1029/1999JC900306>, 2000.

875 Bianchi, D., Dunne, J. P., Sarmiento, J. L., and Galbraith, E. D.: Data-based estimates of suboxia, denitrification,
876 and N₂O production in the ocean and their sensitivities to dissolved O₂, *Global Biogeochem. Cy.*, 26, GB2009,
877 <https://doi.org/10.1029/2011gb004209>, 2012.

878 Blain, S., Quéguiner, B., Armand, L., Belviso, S., Bombled, B., Bopp, L., Bowie, A., Brunet, C., Brussaard, C.,
879 Carlotti, F., Christaki, U., Corbière, A., Durand, I., Ebersbach, F., Fuda, J.-L., Garcia, N., Gerringa, L., Griffiths,
880 B., Guigue, C., Guillermin, C., Jacquet, S., Jeandel, C., Laan, P., Lefèvre, D., Lo Monaco, C., Malits, A., Mosseri,
881 J., Obernosterer, I., Park, Y.-H., Picheral, M., Pondaven, P., Remenyi, T., Sandroni, V., Sarthou, G., Savoye, N.,



- 882 Scouarnec, L., Souhaut, M., Thuiller, D., Timmermans, K., Trull, T., Uitz, J., van Beek, P., Veldhuis, M., Vincent,
883 D., Viollier, E., Vong, L., and Wagener, T.: Effect of natural iron fertilization on carbon sequestration in the
884 Southern Ocean, *Nature*, 446, 1070–1074, <https://doi.org/10.1038/nature05700>, 2007.
- 885 Boss, E. and Behrenfeld, M.: In situ evaluation of the initiation of the North Atlantic phytoplankton bloom,
886 *Geophys. Res. Lett.*, 37, L18603, <https://doi.org/10.1029/2010GL044174>, 2010.
- 887 Boyd, P. W., Jickells, T., Law, C. S., Blain, S., Boyle, E. A., Buesseler, K. O., Coale, K. H., Cullen, J. J., de Baar,
888 H. J. W., Follows, M., Harvey, M., Lancelot, C., Levasseur, M., Owens, N. P. J., Pollard, R., Rivkin, R. B.,
889 Sarmiento, J., Schoemann, V., Smetacek, V., Takeda, S., Tsuda, A., Turner, S., and Watson, A. J.: Mesoscale Iron
890 Enrichment Experiments 1993-2005: Synthesis and Future Directions, *Science*, 315, 612–617,
891 <https://doi.org/10.1126/science.1131669>, 2007.
- 892 Boyd, P. W. and Ellwood, M. J.: The biogeochemical cycle of iron in the ocean, *Nat. Geosci.*, 3, 675–682,
893 <https://doi.org/10.1038/ngeo964>, 2010.
- 894 Buck, K. N., Lohan, M. C., Berger, C. J., and Bruland, K. W.: Dissolved iron speciation in two distinct river
895 plumes and an estuary: Implications for riverine iron supply, *Limnol. Oceanogr.*, 52, 843–855,
896 <https://doi.org/10.4319/lo.2007.52.2.0843>, 2007.
- 897 Canfield, D. E.: The geochemistry of river particulates from the continental USA: Major elements, *Geochim.*
898 *Cosmochim. Ac.*, 61, 3349–3365, [https://doi.org/10.1016/s0016-7037\(97\)00172-5](https://doi.org/10.1016/s0016-7037(97)00172-5), 1997.
- 899 Chen, G., Han, W., Li, Y., Wang, D., and McPhaden, M. J.: Seasonal-to-interannual time-scale dynamics of the
900 equatorial undercurrent in the Indian Ocean, *J. Phys. Oceanogr.*, 45, 1532–1553, [https://doi.org/10.1175/JPO-D-](https://doi.org/10.1175/JPO-D-901)
901 14-0225.1, 2015.
- 902 Chinni, V., Singh, S. K., Bhushan, R., Rengarajan, R., and Sarma, V. V. S. S.: Spatial variability in dissolved iron
903 concentrations in the marginal and open waters of the Indian Ocean, *Marine Chem.*, 208, 11–28,
904 <https://doi.org/10.1016/j.marchem.2018.11.007>, 2019.
- 905 Chinni, V., and Singh, S. K.: Dissolved iron cycling in the Arabian Sea and sub-tropical gyre region of the Indian
906 Ocean, *Geochim. Cosmochim. Ac.*, 317, 325–348, <https://doi.org/10.1016/j.gca.2021.10.026>, 2022.
- 907 Coale, K. H., Johnson, K. S., Fitzwater, S. E., Gordon, R. M., Tanner, S., Chavez, F. P., Ferioli, L., Sakamoto, C.,
908 Rogers, P., Millero, F., Steinberg, P., Nightingale, P., Cooper, D., Cochlan, W. P., Landry, M. R., Constantinou,
909 J., Rollwagen, G., Trasvina, A., and Kudela, R.: A massive phytoplankton bloom induced by an ecosystem-scale
910 iron fertilization experiment in the equatorial Pacific Ocean, *Nature*, 383, 495–501,
911 <https://doi.org/10.1038/383495a0>, 1996.
- 912 Conway, T. M. and John, S. G.: Quantification of dissolved iron sources to the North Atlantic Ocean, *Nature*, 511,
913 212–215, <https://doi.org/10.1038/nature13482>, 2014.
- 914 Dai, A., Qian, T., Trenberth, K. E., and Milliman, J. D.: Changes in continental freshwater discharge from 1948
915 to 2004, *J. Climate*, 22, 2773–2792, <https://doi.org/10.1175/2008JCLI2592.1>, 2009.



- 916 Danabasoglu, G., Bates, S. C., Briegleb, B. P., Jayne, S. R., Jochum, M., Large, W. G., Peacock, S., and Yeager,
917 S. G.: The CCSM4 ocean component, *J. Climate*, 25, 1361–1389, <https://doi.org/10.1175/JCLI-D-11-00091.1>,
918 2012.
- 919 Danabasoglu, G., Lamarque, J.-F., Bacmeister, J., Bailey, D. A., DuVivier, A. K., Edwards, J., Emmons, L. K.,
920 Fasullo, J., Garcia, R., Gettelman, A., Hannay, C., Holland, M. M., Large, W. G., Lauritzen, P. H., Lawrence, D.
921 M., Lenaerts, J. T. M., Lindsay, K., Lipscomb, W. H., Mills, M. J., Neale, R., Oleson, K. W., Otto-Bliesner, B.,
922 Phillips, A. S., Sacks, W., Tilmes, S., van Kampenhout, L., Vertenstein, M., Bertini, A., Dennis, J., Deser, C.,
923 Fischer, C., Fox-Kemper, B., Kay, J. E., Kinnison, D., Kushner, P. J., Larson, V. E., Long, M. C., Mickelson, S.,
924 Moore, J. K., Nienhouse, E., Polvani, L., Rasch, P. J., and Strand, W. G., The Community Earth System Model
925 Version 2 (CESM2), *J. Adv. Model. Earth Syst.*, 12, e2019MS001916, <https://doi.org/10.1029/2019MS001916>,
926 2020.
- 927 de Baar, H. J. W., Boyd, P. W., Coale, K. H., Landry, M. R., Tsuda, A., Assmy, P., Bakker, D. C. E., Bozec, Y.,
928 Barber, R. T., Brzezinski, M. A., Buesseler, K. O., Boye, M., Croot, P. L., Gervais, F., Gorbunov, M. Y., Harrison,
929 P. J., Hiscock, W. T., Laan, P., Lancelot, C., Law, C. S., Lefevre, M., Marchetti, A., Millero, F. J., Nishioka, J.,
930 Nojiri, Y., van Oijen, T., Riebesell, U., Rijkenberg, M. J. A., Saito, H., Takeda, S., Timmermans, K. R., Veldhuis,
931 M. J. W., Waite, A. M., and Wong, C.-S.: Synthesis of iron fertilization experiments: From the Iron Age in the
932 Age of Enlightenment, *J. Geophys. Res.*, 110, C09S16, <https://doi.org/10.1029/2004JC002601>, 2005.
- 933 de Baar, H., Gerringa, L., Laan, P., and Timmermans, K.: Efficiency of carbon removal per added iron in ocean
934 iron fertilization, *Mar. Ecol. Prog. Ser.*, 364, 269–282, <https://doi.org/10.3354/meps07548>, 2008.
- 935 Dohan, K. and Maximenko, N.: Monitoring ocean currents with satellite sensors, *Oceanography*, 23, 94–103,
936 2010.
- 937 Dutkiewicz, S., Ward, B. A., Monteiro, F., and Follows, M. J.: Interconnection between nitrogen fixers and iron
938 in the Pacific Ocean: Theory and numerical model, *Global Biogeochem. Cy.*, 26, GB1012,
939 <https://doi.org/10.1029/2011GB004039>, 2012.
- 940 Elrod, V. A., Berelson, W. M., Coale, K. H., and Johnson, K. S.: The flux of iron from continental shelf sediments:
941 A missing source for global budgets, *Geophys. Res. Lett.*, 31, L12307, <https://doi.org/10.1029/2004GL020216>,
942 2004.
- 943 Flegal, A.R., Smith, G.J., Gill, G.A., Sañudo-Wilhelmy, S., and Anderson, L.C.D.: Dissolved trace element cycles
944 in the San Francisco Bay estuary, *Marine Chem.*, 36, 329–363, 1991.
- 945 Gamo, T., Okamura, K., Hatanaka, H., Hasumoto, H., Komatsu, D., Chinen, M., Mori, M., Tanaka, J., Hirota, A.,
946 and Tsunogai, U.: Hydrothermal plumes in the Gulf of Aden, as characterized by light transmission, Mn, Fe, CH₄
947 and delta C-13-CH₄ anomalies, *Deep-Sea Res. Pt. II*, 121, 62–70, 2015.
- 948 Garcia, H. E., Locarnini, R. A., Boyer, T. P., Antonov, J. I., Baranova, O. K., Zweng, M. M., Reagan, J. R., and
949 Johnson, D. R.: World Ocean Atlas 2013, Volume 3: Dissolved Oxygen, Apparent Oxygen Utilization, and
950 Oxygen Saturation, edited by: Levitus, S. and Mishonov, A., NOAA Atlas NESDIS, 75, 27 pp., 2014a.



- 951 Garcia, H. E., Locarnini, R. A., Boyer, T. P., Antonov, J. I., Baranova, O. K., Zweng, M. M., Reagan, J. R., and
952 Johnson, D. R.: World Ocean Atlas 2013, Volume 4: Dissolved Inorganic Nutrients (phosphate, nitrate, silicate),
953 edited by: Levitus, S. and Mishonov, A., NOAA Atlas NESDIS, 76, 25 pp., 2014b.
- 954 Garcia H. E., Boyer, T. P., Baranova, O. K., Locarnini, R. A., Mishonov, A. V., Grodsky, A., Paver, C. R.,
955 Weathers, K. W., Smolyar, I. V., Reagan, J. R., Seidov, D., Zweng, M. M.: World Ocean Atlas 2018: Product
956 Documentation, edited by: Mishonov, A., 2019.
- 957 Geider, R. J. and La Roche, J.: The role of iron in phytoplankton photosynthesis, and the potential for iron-
958 limitation of primary productivity in the sea, *Photosynth. Res.*, 39, 275–301, <https://doi.org/10.1007/bf00014588>,
959 1994.
- 960 Gent, P. R. and McWilliams, J. C.: Isopycnal mixing in ocean circulation models, *J. Phys. Oceanogr.*, 20, 150–
961 155, [https://doi.org/10.1175/1520-0485\(1990\)020<0150:IMIOCM>2.0.CO;2](https://doi.org/10.1175/1520-0485(1990)020<0150:IMIOCM>2.0.CO;2), 1990.
- 962 Grand, M. M., Measures, C. I., Hatta, M., Hiscock, W. T., Buck, C. S., and Landing, W. M.: Dust deposition in
963 the eastern Indian Ocean: The ocean perspective from Antarctica to the Bay of Bengal, *Global Biogeochem.*
964 *Cycles*, 29, 357–374, <https://doi.org/10.1002/2014gb004898>, 2015.
- 965 Guieu, C., Al Azhar, M., Aumont, O., Mahowald, N., Lévy, M., Éthé, C., and Lachkar, Z.: Major impact of dust
966 deposition on the productivity of the Arabian Sea, *Geophys. Res. Lett.*, 46, 6736–6744, 2019
- 967 Gustafsson, O., Kruså, M., Zencak, Z., Sheesley, R. J., Granat, L., Engström, E., Praveen, P. S., Rao, P. S., Leck,
968 C., and Rodhe, H.: Brown clouds over South Asia: biomass or fossil fuel combustion?, *Science*, 323, 495–498,
969 <https://doi.org/10.1126/science.1164857>, 2009.
- 970 Haake, B., Ittekkot, V., Rixen, T., Ramaswamy, V., Nair, R. R., and Curry, W. B.: Seasonality and interannual
971 variability of particle fluxes to the deep Arabian Sea, *Deep-Sea Res. Pt. I*, 40, 1323–1344, 1993.
- 972 Han, W., McCreary, J. P., Anderson, D. L. T., and Mariano, A. J.: Dynamics of the eastern surface jets in the
973 equatorial Indian Ocean, *J. Phys. Oceanogr.*, 29, 2191–2209, [https://doi.org/10.1175/1520-
974 0485\(1999\)029<2191:DOTESJ>2.0.CO;2](https://doi.org/10.1175/1520-0485(1999)029<2191:DOTESJ>2.0.CO;2), 1999.
- 975 Holte, J., Talley, L. D., Gilson, J., and Roemmich, D.: An Argo mixed layer climatology and database, *Geophys.*
976 *Res. Lett.*, 44, 5618–5626, <https://doi.org/10.1002/2017GL073426>, 2017.
- 977 Huffman, G. J., Adler, R. F., Arkin, P., Chang, A., Ferraro, R., Gruber, A., Janowiak, J., McNab, A., Rudolf, B.,
978 and Schneider, U.: The Global Precipitation Climatology Project (GPCP) Combined Precipitation Dataset, *B. Am.*
979 *Meteorol. Soc.*, 78, 5–20, [https://doi.org/10.1175/1520-0477\(1997\)078<0005:TGPCPG>2.0.CO;2](https://doi.org/10.1175/1520-0477(1997)078<0005:TGPCPG>2.0.CO;2), 1997.
- 980 Ilyina, T., Six, K. D., Segschneider, J., Maier-Reimer, E., Li, H., and Núñez-Riboni, I.: Global ocean
981 biogeochemistry model HAMOCC: Model architecture and performance as component of the MPI-Earth system
982 model in different CMIP5 experimental realizations, *J. Adv. Model. Earth Sy.*, 5, 287–315,
983 <https://doi.org/10.1029/2012MS000178>, 2013.



- 984 Jickells, T. D., An, Z. S., Andersen, K. K., Baker, A. R., Bergametti, G., Brooks, N., Cao, J. J., Boyd, P. W., Duce,
985 R. A., Hunter, K. A., Kawahata, H., Kubilay, N., laRoche, J., Liss, P. S., Mahowald, N., Prospero, J. M., Ridgwell,
986 A. J., Tegen, I., and Torres, R.: Global Iron Connections between Desert Dust, Ocean Biogeochemistry, and
987 Climate, *Science*, 308, 67–71, 2005.
- 988 Jin, Q., Wei, J., Pu, B., Yang, Z. L., and Parajuli, S. P.: High summertime aerosol loadings over the Arabian Sea
989 and their transport pathways, *J. Geophys. Res.-Atmos.*, 123, 10568–10590,
990 <https://doi.org/10.1029/2018jd028588>, 2018.
- 991 Johnson, K. S., Chavez, F. P., and Friederich, G. E.: Continental-shelf sediment as a primary source of iron for
992 coastal phytoplankton, *Nature*, 398, 697–700, <https://doi.org/10.1038/19511>, 1999.
- 993 Kalnay, E., Kanamitsu, M., Kistler, R., Collins, W., Deaven, D., Gandin, L., Iredell, M., Saha, S., White, G.,
994 Woollen, J., Zhu, Y., Leetmaa, A., Reynolds, R., Chelliah, M., Ebisuzaki, W., Higgins, W., Janowiak, J., Mo, K.
995 C., Ropelewski, C., Wang, J., Jenne, R., and Joseph, D.: The NCEP/NCAR 40-Year Reanalysis Project, *B. Am.*
996 *Meteorol. Soc.*, 77, 437–471, [https://doi.org/10.1175/1520-0477\(1996\)077<0437:TNYRP>2.0.CO;2](https://doi.org/10.1175/1520-0477(1996)077<0437:TNYRP>2.0.CO;2), 1996.
- 997 Kawamiya, M. and Oschlies, A.: Formation of a basin-scale surface chlorophyll pattern by Rossby waves,
998 *Geophys. Res. Lett.*, 28, 4139–4142, 2001.
- 999 Kohfeld, K. E. and Harrison, S. P.: DIRTMAP: the geological record of dust, *Earth-Science Rev.*, 54, 81–114,
1000 [https://doi.org/10.1016/S0012-8252\(01\)00042-3](https://doi.org/10.1016/S0012-8252(01)00042-3), 2001.
- 1001 Kok, J. F., Adebisi, A. A., Albani, S., Balkanski, Y., Checa-Garcia, R., Chin, M., Colarco, P. R., Hamilton, D. S.,
1002 Huang, Y., Ito, A., Klose, M., Li, L., Mahowald, N. M., Miller, R. L., Obiso, V., Pérez García-Pando, C., Rocha-
1003 Lima, A., and Wan, J. S.: Contribution of the world's main dust source regions to the global cycle of desert dust,
1004 *Atmos. Chem. Phys.*, 21, 8169–8193, <https://doi.org/10.5194/acp-21-8169-2021>, 2021.
- 1005 Koňe, V., Aumont, O., Lévy, M., and Resplandy, L.: Physical and Biogeochemical Controls of the Phytoplankton
1006 Seasonal Cycle in the Indian Ocean: A Modeling Study, *Geoph. Monog. Series*, 185, 147–166,
1007 <https://doi.org/10.1029/2008GM000700>, 2009.
- 1008 Kumar, A., Suresh, K., and Rahaman, W.: Geochemical Characterization of Modern Aeolian Dust over the
1009 Northeastern Arabian Sea: Implication for Dust Transport in the Arabian Sea, *Science of the Total Environment*,
1010 729, 138576, <https://doi.org/10.1016/j.scitotenv.2020.138576>, 2020.
- 1011 Kuttippurath, J., Sunanda, N., Martin, M. V., and Chakraborty, K.: Tropical storms trigger phytoplankton blooms
1012 in the deserts of north Indian Ocean, *NPJ Climate and Atmospheric Science*, 4, 11,
1013 <https://doi.org/10.1038/s41612-021-00166-x>, 2021.
- 1014 Large, W. G., McWilliams, J. C., and Doney, S. C.: Oceanic vertical mixing: A review and a model with a
1015 nonlocal boundary layer parameterization, *Rev. Geophys.*, 32, 363–403, 1994.
- 1016 Large, W. G. and Yeager, S. G.: The global climatology of an interannually varying air-sea flux data set, *Clim.*
1017 *Dynam.*, 33, 341–364, <https://doi.org/10.1007/s00382-008-0441-3>, 2009.



- 1018 Léon, J. F. and Legrand, M.: Mineral dust sources in the surroundings of the North Indian Ocean, *Geophys. Res.*
1019 *Let.*, 30, 1309, <https://doi.org/10.1029/2002GL016690>, 2003.
- 1020 Letelier, R. M., Karl, D. M., Abbott, M. R., and Bidigare, R. R.: Light driven seasonal patterns of chlorophyll and
1021 nitrate in the lower euphotic zone of the North Pacific Subtropical Gyre, *Limnol. Oceanogr.*, 49, 508–519,
1022 <https://doi.org/10.4319/lo.2004.49.2.0508>, 2004.
- 1023 Lévy, M., Shankar, D., André, J., Shenoi, S., Durand, F., and de Boyer Montégut, C.: Basin-wide seasonal
1024 evolution of the Indian Ocean's phytoplankton blooms, *J. Geophys. Res.-Oceans*, 112, C12014,
1025 <https://doi.org/10.1029/2007JC004090>, 2007.
- 1026 Liu, J. P., Xue, Z., Ross, K., Wang, H. J., Yang, Z. S., and Gao, S.: Fate of sediments delivered to the sea by Asian
1027 large rivers: Long-distance transport and formation of remote alongshore clinothems, *The Sedimentary Record*,
1028 7(4), 4–9, <https://doi.org/10.2110/sedred.2009.4.4>, 2009.
- 1029 Liu, X., Ma, P.-L., Wang, H., Tilmes, S., Singh, B., Easter, R. C., Ghan, S. J., and Rasch, P. J.: Description and
1030 evaluation of a new four-mode version of the Modal Aerosol Module (MAM4) within version 5.3 of the
1031 Community Atmosphere Model, *Geosci. Model Dev.*, 9, 505–522, <https://doi.org/10.5194/gmd-9-505-2016>,
1032 2016.
- 1033 Long, M. C., Moore, J. K., Lindsay, K., Levy, M. N., Doney, S. C., Luo, J. Y., Krumhardt, K. M., Letscher, R.
1034 T., Grover, M., and Sylvester, Z. T.: Simulations with the Marine Biogeochemistry Library (MARBL), *J. Adv.*
1035 *Model. Earth Syst.*, accepted, <https://doi.org/10.1029/2021MS002647>, 2021.
- 1036 Madhu, N., Jyothibabu, R., Maheswaran, P., Gerson, V. J., Gopalakrishnan, T., and Nair, K.: Lack of seasonality
1037 in phytoplankton standing stock (chlorophyll a) and production in the western Bay of Bengal, *Cont. Shelf Res.*,
1038 26, 1868–1883, 2006.
- 1039 Madhupratap, M., Prasanna Kumar, S., Bhattathiri, P. M. A., DileepKumar, M., Raghukumar, S., Nair, K. K. C.,
1040 and Ramaiah, N.: Mechanism of the biological response to winter cooling in the northeastern Arabian Sea, *Nature*,
1041 384, 549–552, 1996.
- 1042 Madhupratap, M., Gauns, M., Ramaiah, N., Kumar, S. P., Muraleedharan, P., de Sousa, S., Sardesai, S., and
1043 Muraleedharan, U.: Biogeochemistry of the Bay of Bengal: physical, chemical and primary productivity
1044 characteristics of the central and western Bay of Bengal during summer monsoon 2001, *Deep-Sea Res. Pt. II*, 50,
1045 881–896, [https://doi.org/10.1016/S0967-0645\(02\)00611-2](https://doi.org/10.1016/S0967-0645(02)00611-2), 2003.
- 1046 Mahowald, N. M., Engelstaedter, S., Luo, C., Sealy, A., Artaxo, P., Benitez-Nelson, C., Bonnet, S., Chen, Y.,
1047 Chuang, P. Y., Cohen, D. D., Dulac, F., Herut, B., Johansen, A. M., Kubilay, N., Losno, R., Maenhaut, W., Paytan,
1048 A., Prospero, J. M., Shank, L. M., and Siefert, R. L.: Atmospheric iron deposition: global distribution, variability,
1049 and human perturbations, *Ann. Rev. Mar. Sci.*, 1, 245–278,
1050 <https://doi.org/10.1146/annurev.marine.010908.163727>, 2009.
- 1051 Masumoto, Y. and Meyers, G.: Forced Rossby waves in the southern tropical Indian Ocean, *J. Geophys. Res.-*
1052 *Oceans*, 103, 27589–27602, <https://doi.org/10.1029/98JC02546>, 1998.



- 1053 Mayorga, E., Seitzinger, S. P., Harrison, J. A., Dumont, E., Beusen, A. H. W., Bouwman, A. F., Fekete, B. M.,
1054 Kroeze, C. and van Drecht, G.: Global Nutrient Export from WaterSheds 2 (NEWS 2): Model development and
1055 implementation, *Environ. Modell. Softw.*, 25, 837–853, <https://doi.org/10.1016/j.envsoft.2010.01.007>, 2010.
- 1056 McLennan, S. M.: Relationships between the trace element composition of sedimentary rocks and upper
1057 continental crust, *Geochemistry, Geophysics, Geosystems*, 2(4), 1021, <http://doi.org/10.1029/2000gc000109>,
1058 2001.
- 1059 McPhaden, M. J., Wang, Y., and Ravichandran, M.: Volume transports of the Wyrтки jets and their relationship
1060 to the Indian Ocean dipole, *J. Geophys. Res.-Oceans*, 120, 5302–5317, 2015.
- 1061 Measures, C. I. and Vink, S.: Seasonal variations in the distribution of Fe and Al in the surface waters of the
1062 Arabian Sea, *Deep-Sea Res. Pt. II*, 46, 1597–1622, 1999.
- 1063 Mills, M. M., Ridame, C., Davey, M., La Roche, J., and Geider, R. J.: Iron and phosphorus co-limit nitrogen
1064 fixation in the eastern tropical North Atlantic, *Nature*, 429, 292, <https://doi.org/10.1038/nature02550>, 2004.
- 1065 Moffett, J. W., Goepfert, T. J., and Naqvi, S. W. A.: Reduced iron associated with secondary nitrite maxima in
1066 the Arabian Sea, *Deep-Sea Res. Pt. I*, 54, 1341–1349, <https://doi.org/10.1016/j.dsr.2007.04.004>, 2007.
- 1067 Moffett, J. W., Vedamati, J., Goepfert, T. J., Pratihary, A., Gauns, M., and Naqvi, S. W. A.: Biogeochemistry of
1068 iron in the Arabian Sea, *Limnol. Oceanogr.*, 60, 1671–1688, <https://doi.org/10.1002/lno.10132>, 2015.
- 1069 Moore, J. K., Doney, S. C., and Lindsay, K.: Upper ocean ecosystem dynamics and iron cycling in a global three-
1070 dimensional model, *Global Biogeochem. Cy.*, 18, GB4028, <https://doi.org/10.1029/2004GB002220>, 2004.
- 1071 Moore, J. K. and Braucher, O.: Sedimentary and mineral dust sources of dissolved iron to the world ocean,
1072 *Biogeosciences*, 5, 631–656, <https://doi.org/10.5194/bg-5-631-2008>, 2008.
- 1073 Moore, C. M., Mills, M. M., Achterberg, E. P., Geider, R. J., La Roche, J., Lucas, M. I., McDonagh, E. I., Pan,
1074 X., Poulton, A. J., and Rijkenberg, M. J.: Large-scale distribution of Atlantic nitrogen fixation controlled by iron
1075 availability, *Nat. Geosci.*, 2, 867–871, 2009.
- 1076 Moore, C. M., Mills, M. M., Arrigo, K. R., Berman-Frank, I., Bopp, L., Boyd, P. W., Galbraith, E. D., Geider,
1077 R. J., Guieu, C., Jaccard, S. L., Jickells, T. D., Roche, J. L., Lenton, T. M., Mahowald, N. M., Marañón, E.,
1078 Marinov, I., Moore, J. K., Nakatsuka, T., Oschlies, A., Saito, M. A., Thingstad, T. F., Tsuda, A., and Ulloa, O.:
1079 Processes and patterns of oceanic nutrient limitation, *Nat. Geosci.*, 6, 701–710,
1080 <https://doi.org/10.1038/NGEO1765>, 2013a.
- 1081 Moore, J. K., Lindsay, K., Doney, S. C., Long, M. C., and Misumi, K.: Marine Ecosystem Dynamics and
1082 Biogeochemical Cycling in the Community Earth System Model CESM1(BGC): Comparison of the 1990s with
1083 the 2090s under the RCP4.5 and RCP8.5 Scenarios, *J. Climate*, 26, 9291–9312, <https://doi.org/10.1175/jcli-d-12-1084>
1084 00566.1, 2013b.



- 1085 Moorthy, K. K. and Babu, S. S.: Aerosol black carbon over Bay of Bengal observed from an island location, Port
1086 Blair: Temporal features and long-range transport, *J. Geophys. Res.*, 111, D17205, doi:10.1029/2005JD006855,
1087 2006.
- 1088 Morrison, J. M., Codispoti, L. A., Smith, S. L., Wishner, K., Flagg, C., Gardner, W. D., Gaurin, S., Naqvi, S.,
1089 Manghnani, V., Prosperie, L., and Gundersen, J. S.: The oxygen minimum zone in the Arabian Sea during 1995,
1090 *Deep-Sea Res. Pt. II*, 46, 1903–1931, 1999.
- 1091 Morrison, J. M., Codispoti, L. A., Gaurin, S., Jones, B., Manghanani, V., and Zheng, Z.: Seasonal variations of
1092 hydrographic and nutrient fields during the US JGOFS Arabian Sea Process Study, *Deep-Sea Res. Pt. II*, 45,
1093 2053–2101, 1998.
- 1094 Naqvi, S. W. A., Moffett, J. W., Gauns, M. U., Narvekar, P. V., Pratihary, A. K., Naik, H., Shenoy, D. M.,
1095 Jayakumar, D. A., Goepfert, T. J., Patra, P. K., Al-Azri, A., and Ahmed, S. I.: The Arabian Sea as a high-nutrient,
1096 low-chlorophyll region during the late Southwest Monsoon, *Biogeosciences*, 7, 2091–2100,
1097 <https://doi.org/10.5194/bg-7-2091-2010>, 2010.
- 1098 Nishioka, J., Obata, H., and Tsumune, D.: Evidence of an extensive spread of hydrothermal dissolved iron in the
1099 Indian Ocean, *Earth Planet. Sci. Lett.*, 361, 26–33, <https://doi.org/10.1016/j.epsl.2012.11.040>, 2013.
- 1100 Olsen, A., Key, R. M., van Heuven, S., Lauvset, S. K., Velo, A., Lin, X., Schirmick, C., Kozyr, A., Tanhua, T.,
1101 Hoppema, M., Jutterström, S., Steinfeldt, R., Jeansson, E., Ishii, M., Pérez, F. F., and Suzuki, T.: The Global
1102 Ocean Data Analysis Project version 2 (GLODAPv2) – an internally consistent data product for the world ocean,
1103 *Earth Syst. Sci. Data*, 8, 297–323, <https://doi.org/10.5194/essd-8-297-2016>, 2016.
- 1104 Périgaud, C., and Delecluse, P.: Annual sea level variations in the southern tropical Indian Ocean from Geosat
1105 and shallow water simulations, *J. Geophys. Res.*, 97, 20169–20178, <https://doi.org/10.1029/92JC01961>, 1992.
- 1106 Pham, A. L. D., and Ito, T.: Anthropogenic iron deposition alters the ecosystem and carbon balance of the Indian
1107 Ocean over a centennial timescale, *J. Geophys. Res.-Oceans*, 126, e2020JC016475,
1108 <https://doi.org/10.1029/2020JC016475>, 2021.
- 1109 Pollard, R. T., Salter, I., Sanders, R. J., Lucas, M. I., Moore, C. M., Mills, R. A., Statham, P. J., Allen, J. T., Baker,
1110 A. R., Bakker, D. C. E., Charette, M. A., Fielding, S., Fones, G. R., French, M., Hickman, A. E., Holland, R. J.,
1111 Hughes, J. A., Jickells, T. D., Lampitt, R. S., Morris, P. J., Nedelec, F. H., Nielsdottir, M., Planquette, H., Popova,
1112 E. E., Poulton, A. J., Read, J. F., Seeyave, S., Smith, T., Stinchcombe, M., Taylor, S., Thomalla, S., Venables, H.
1113 J., Williamson, R., and Zubkov, M. V.: Southern Ocean deep-water carbon export enhanced by natural iron
1114 fertilization, *Nature*, 457, 577–580, <https://doi.org/10.1038/nature07716>, 2009.
- 1115 Prasanna Kumar, S., Madhupratap, M., Dileep Kumar, M., Muraleedharan, P. M., de Souza, S. N., Gauns, M.,
1116 and Sarma, V. V. S. S.: High biological productivity in the central Arabian Sea during summer monsoon driven
1117 by Ekman pumping and lateral advection, *Curr. Sci.*, 81, 1633–1638, 2001.



- 1118 Prasanna Kumar, S., Nuncio, M., Narvekar, J., Kumar, A., Sardesai, S., de Souza, S. N., Gauns, M., Ramaiah, N.,
1119 and Madhupratap, M.: Are eddies nature's trigger to enhance biological productivity in the Bay of Bengal?,
1120 *Geophys. Res. Lett.*, 31, L07309, <https://doi.org/10.1029/2003GL019274>, 2004.
- 1121 Prasanna Kumar, S., Divya David, T., Byju, P., Narvekar, J., Yoneyama, K., Nakatani, N., Ishida, A., Horii, T.,
1122 Masumoto, Y., and Mizuno, K.: Bio-physical coupling and ocean dynamics in the central equatorial Indian Ocean
1123 during 2006 Indian Ocean Dipole, *Geophys. Res. Lett.*, 39, L14601, doi:10.1029/2012GL052609, 2012.
- 1124 Ramaswamy, V. and Gaye, B.: Regional variations in the fluxes of foraminifera carbonate, coccolithophorid
1125 carbonate and biogenic opal in the northern Indian Ocean, *Deep-Sea Res. Pt. I*, 53, 271–293,
1126 doi:10.1016/j.dsr.2005.11.003, 2006.
- 1127 Ramaswamy, V., Gaye, B., Shirodkar, P. V., Rao, P. S., Chivas, A. R., Wheeler, D., and Thwin, S.: Distribution
1128 and sources of organic carbon, nitrogen and their isotopic signatures in sediments from the Ayeyarwady
1129 (Irrawaddy) continental shelf, northern Andaman Sea, *Marine Chem.*, 111(3), 137–150.
1130 <https://doi.org/10.1016/j.marchem.2008.04.006>, 2008.
- 1131 Raven, J. A.: The iron and molybdenum use efficiencies of plant growth with different energy, carbon and nitrogen
1132 sources, *New Phytol.*, 109, 279–287, <https://doi.org/10.1111/j.1469-8137.1988.tb04196.x>, 1988.
- 1133 Redi, M. H.: Oceanic isopycnal mixing by coordinate rotation, *J. Phys. Oceanogr.*, 12, 1154–1158,
1134 [https://doi.org/10.1175/1520-0485\(1982\)012<1154:OIMBCR>2.0.CO;2](https://doi.org/10.1175/1520-0485(1982)012<1154:OIMBCR>2.0.CO;2), 1982.
- 1135 Resplandy, L., Lévy, M., Madec, G., Pous, S., Aumont, O., and Kumar, D.: Contribution of mesoscale processes
1136 to nutrient budgets in the Arabian Sea, *J. Geophys. Res.*, 116, C11007, <https://doi.org/10.1029/2011JC007006>,
1137 2011.
- 1138 Rixen, T., Gaye, B., and Emeis, K.-C.: The monsoon, carbon fluxes, and the organic carbon pump in the northern
1139 Indian Ocean, *Prog. Oceanogr.*, 175, 24–39, <https://doi.org/10.1016/j.pocean.2019.03.001>, 2019.
- 1140 Robinson, R. A. J., Bird, M. I., Oo, N. W., Hoey, T. B., Aye, M. M., Higgitt, D. L., Lud, X. X., Swe, A., Tun, T.,
1141 and Win, S. L.: The Irrawaddy river sediment flux to the Indian Ocean: the original nineteenth-century data
1142 revisited, *J. Geol.*, 115, 629–640, <https://doi.org/10.1086/521607>, 2007.
- 1143 Sathyendranath, S., Brewin, R. J., Brockmann, C., Brotas, V., Calton, B., Chuprin, A., Cipollini, P., Couto, A. B.,
1144 Dingle, J., Doerffer, R., Donlon, C., Dowell, M., Farman, A., Grant, M., Groom, S., Horseman, A., Jackson, T.,
1145 Krasemann, H., Lavender, S., Martinez-Vicente, V., Mazeran, C., Mélin, F., Moore, T. S., Müller, D., Regner, P.,
1146 Roy, S., Steele, C. J., Steinmetz, F., Swinton, J., Taberner, M., Thompson, A., Valente, A., Zühlke, M.,
1147 Brando, V. E., Feng, H., Feldman, G., Franz, B. A., Frouin, R., Gould, R. W., Hooker, S. B., Kahru, M.,
1148 Kratzer, S., Mitchell, B. G., Muller-Karger, F. E., Sosik, H. M., Voss, K. J., Werdell, J., and Platt, T.: An Ocean-
1149 Colour Time Series for Use in Climate Studies: The Experience of the Ocean-Colour Climate Change Initiative
1150 (OC-CCI), *Sensors*, 19, 4285, <https://doi.org/10.3390/s19194285>, 2019.



- 1151 Schlitzer, R., Masferrer Dodas, E., Adjou, M., Anderson, R. F., Andre, F., Cockwell, D. M., et al.: The
1152 GEOTRACES Intermediate Data Product 2021 (IDP2021), NERC EDS British Oceanographic Data Centre NOC,
1153 doi: 10.5285/cf2d9ba9-d51d-3b7c-e053-8486abc0f5fd, 2021.
- 1154 Schlosser, C., Klar, J. K., Wake, B. D., Snow, J. T., Honey, D. J., Woodward, E. M. S., Lohan, M. C., Achterberg,
1155 E. P., and Moore, C. M.: Seasonal ITCZ migration dynamically controls the location of the (sub)tropical Atlantic
1156 biogeochemical divide, *P. Natl. Acad. Sci. USA*, 111, 1438–1442, 2014.
- 1157 Schmidtko, S., Stramma, L., and Visbeck, M.: Decline in global oceanic oxygen content during the past five
1158 decades, *Nature*, 542, 335–339, <https://doi.org/10.1038/nature21399>, 2017.
- 1159 Schott, F. and McCreary, J. P.: The monsoon circulation of the Indian Ocean, *Prog. Oceanogr.*, 51, 1–123,
1160 [https://doi.org/10.1016/S0079-6611\(01\)00083-0](https://doi.org/10.1016/S0079-6611(01)00083-0), 2001.
- 1161 Sedwick, P. N. and DiTullio, G. R.: Regulation of algal blooms in Antarctic shelf waters by the release of iron
1162 from melting sea ice, *Geophys. Res. Lett.*, 24, 2515–2518, <https://doi.org/10.1029/97GL02596>, 1997.
- 1163 Singh, N. D., Chinni, V., and Singh, S. K.: Dissolved aluminium cycling in the northern, equatorial and subtropical
1164 gyre region of the Indian Ocean, *Geochim. Cosmochim. Ac.*, 268, 160–185, doi: 10.1016/j.gca.2019.09.028, 2020.
- 1165 Sholkovitz, E. R.: The flocculation of dissolved Fe, Mn, Al, Cu, Ni, Co and Cd during estuarine mixing, *Earth
1166 Planet. Sc. Lett.*, 41, 77–86, [https://doi.org/10.1016/0012-821X\(78\)90043-2](https://doi.org/10.1016/0012-821X(78)90043-2), 1978.
- 1167 Sholkovitz, E. R., Sedwick, P. N., Church, T. M., Baker, A. R., and Powell, C. F.: Fractional solubility of aerosol
1168 iron: Synthesis of a global-scale data set, *Geochim. Cosmochim. Ac.*, 89, 173–189,
1169 <https://doi.org/10.1016/j.gca.2012.04.022>, 2012.
- 1170 Smith, R., Jones, P., Briegleb, B., Bryan, F., Danabasoglu, G., Dennis, J., Dukowicz, J., Eden, C., Fox-Kemper,
1171 B., Gent, P., Hecht, M., Jayne, S., Jochum, M., Large, W., Lindsay, K., Maltrud, M., Norton, N., Peacock, S.,
1172 Vertenstein, M., and Yeager, S.: The Parallel Ocean Program (POP) reference manual, Ocean component of the
1173 Community Climate System Model (CCSM), LANL Tech. Report, LAUR-10-01853, 141 pp., 2010.
- 1174 Smith, S. L.: Understanding the Arabian Sea: Reflections on the 1994-1996 Arabian Sea Expedition, *Deep-Sea
1175 Res. Pt. II*, 48, 1385–1402, 2001.
- 1176 Srinivas, B., Sarin, M. M., and Kumar, A.: Impact of anthropogenic sources on aerosol iron solubility over the
1177 Bay of Bengal and the Arabian Sea, *Biogeochemistry*, 110, 257–268, <https://doi.org/10.1007/s10533-011-9680-1>,
1178 2012.
- 1179 Srinivas, B. and Sarin, M. M.: Atmospheric dry-deposition of mineral dust and anthropogenic trace metals to the
1180 Bay of Bengal, *J. Mar. Syst.*, 126, 56–68, <https://doi.org/10.1016/j.jmarsys.2012.11.004>, 2013.



- 1181 Strutton, P. G., Coles, V. J., Hood, R. R., Matear, R. J., McPhaden, M. J., and Phillips, H. E.: Biogeochemical
1182 variability in the central equatorial Indian Ocean during the monsoon transition, *Biogeosciences*, 12, 2367–2382,
1183 <https://doi.org/10.5194/bg-12-2367-2015>, 2015.
- 1184 Sunda, W. G. and Huntsman, S. A.: Iron uptake and growth limitation in oceanic and coastal phytoplankton, *Mar.*
1185 *Chem.*, 50, 189–206, [https://doi.org/10.1016/0304-4203\(95\)00035-P](https://doi.org/10.1016/0304-4203(95)00035-P), 1995.
- 1186 Tagliabue, A., Bopp, L., Dutay, J.-C., Bowie, A. R., Chever, F., Jean-Baptiste, P., Bucciarelli, E., Lannuzel, D.,
1187 Remenyi, T., Sarthou, G., Aumont, O., Gehlen, M., and Jeandel, C.: Hydrothermal contribution to the oceanic
1188 dissolved iron inventory, *Nat. Geosci.*, 3, 252–256, <https://doi.org/10.1038/ngeo818>, 2010.
- 1189 Tagliabue, A., Mtshali, T., Aumont, O., Bowie, A. R., Klunder, M. B., Roychoudhury, A. N., and Swart, S.: A
1190 global compilation of dissolved iron measurements: focus on distributions and processes in the Southern Ocean,
1191 *Biogeosciences*, 9, 2333–2349, <https://doi.org/10.5194/bg-9-2333-2012>, 2012.
- 1192 Tagliabue, A., Aumont, O., and Bopp, L.: The impact of different external sources of iron on the global carbon
1193 cycle, *Geophys. Res. Lett.*, 41, 920–926, <https://doi.org/10.1002/2013GL059059>, 2014.
- 1194 Tagliabue, A., Aumont, O., De'Ath, R., Dunne, J. P., Dutkiewicz, S., Galbraith, E., Misumi, K., Moore, J. K.,
1195 Ridgwell, A., Sherman, E., Stock, C., Vichi, M., Völker, C., and Yool, A.: How well do global ocean
1196 biogeochemistry models simulate dissolved iron distributions?, *Global Biogeochem. Cy.*, 30, 2,
1197 <https://doi.org/10.1002/2015GB005289>, 2016.
- 1198 Takeda, S., Kamarani, A., and Kawanobe, K.: Effects of nitrogen and iron enrichments on phytoplankton
1199 communities, *Mar. Chem.*, 50, 229–241, [https://doi.org/10.1016/0304-4203\(95\)00038-S](https://doi.org/10.1016/0304-4203(95)00038-S), 1995.
- 1200 Thushara, V., Vinayachandran, P. N. M., Matthews, A. J., Webber, B. G. M., and Queste, B. Y.: Vertical
1201 distribution of chlorophyll in dynamically distinct regions of the southern Bay of Bengal, *Biogeosciences*, 16,
1202 1447–1468, <https://doi.org/10.5194/bg-16-1447-2019>, 2019.
- 1203 Twining, B. S., Rauschenberg, S., Baer, S. E., Lomas, M. W., Martiny, A. C., and Antipova, O. M.: A nutrient
1204 limitation mosaic in the eastern tropical Indian Ocean, *Deep-Sea Res. Pt. II*, 166, 125–140,
1205 <https://doi.org/10.1016/j.dsr2.2019.05.001>, 2019.
- 1206 Unger, D., Ittekkot, V., Schäfer, P., Tiemann, J., and Reschke, S.: Seasonality and interannual variability of
1207 particle fluxes to the deep Bay of Bengal: influence of riverine input and oceanographic processes, *Deep-Sea Res.*
1208 *Pt. II*, 50, 897–923, 2003.
- 1209 Vialard, J., Duvel, J. P., McPhaden, M. J., Bouruet-Aubertot, P., Ward, B., Key, E., Bourras, D., Weller, R.,
1210 Minnett, P., Weill, A., Cassou, C., Eymard, L., Fristedt, T., Basdevant, C., Dandonneau, Y., Duteil, O., Izumo,
1211 T., de Boyer Montégut, C., Masson, S., and Kennan, S.: Cirene: Air – Sea Interactions in the Seychelles – Chagos
1212 Thermocline Ridge Region, *B. Am. Meteor. Soc.*, 90, 45–62, <https://doi.org/10.1175/2008BAMS2499.1>, 2009.
- 1213 Vidya, P. J. and Prasanna Kumar, S.: Role of mesoscale eddies on the variability of biogenic flux in the northern
1214 and central Bay of Bengal, *J. Geophys. Res.-Oceans*, 118, 5760–5771, <https://doi.org/10.1002/jgrc.20423>, 2013.



- 1215 Vidya, P. J., Prasanna Kumar, S., Gauns, M., Verenkar, A., Unger, D., and Ramaswamy, V.: Influence of physical
1216 and biological processes on the seasonal cycle of biogenic flux in the equatorial Indian Ocean, *Biogeosciences*,
1217 10, 7493–7507, <https://doi.org/10.5194/bg-10-7493-2013>, 2013.
- 1218 Vinayachandran, P. N., Chauhan, P., Mohan, M., and Nayak, S.: Biological response of the sea around Sri Lanka
1219 to summer monsoon, *Geophys. Res. Lett.*, 31, L01302, <https://doi.org/10.1029/2003GL018533>, 2004.
- 1220 Vinayachandran, P. N., Shankar, D., Vernekar, S., Sandeep, K. K., Amol, P., Neema, C. P., and Chatterjee, A.: A
1221 summer monsoon pump to keep the Bay of Bengal salty, *Geophys. Res. Lett.*, 40, 1777–1782,
1222 <https://doi.org/10.1002/grl.50274>, 2013.
- 1223 Vu, H. and Sohrin, Y.: Diverse stoichiometry of dissolved trace metals in the Indian Ocean, *Sci. Rep.*, 3,
1224 [doi:10.1038/srep01745](https://doi.org/10.1038/srep01745), 2013.
- 1225 Wang, S., Bailey, D., Lindsay, K., Moore, J. K., and Holland, M.: Impact of sea ice on the marine iron cycle and
1226 phytoplankton productivity, *Biogeosciences*, 11, 4713–4731, <https://doi.org/10.5194/bg-11-4713-2014>, 2014.
- 1227 Webber, B. G. M., Matthews, A. J., Vinayachandran, P. N., Neema, C. P., Sanchez-Franks, A., Vijith, V., Amol,
1228 P., and Baranowski, D. B.: The dynamics of the Southwest Monsoon current in 2016 from high-resolution in situ
1229 observations and models, *J. Phys. Oceanogr.*, 48, 2259–2282, <https://doi.org/10.1175/JPO-D-17-0215.1>, 2018.
- 1230 Wiggert, J. D., and Murtugudde, R. G.: The sensitivity of the Southwest Monsoon phytoplankton bloom to
1231 variations in aeolian iron deposition over the Arabian Sea, *J. Geophys. Res.*, 112, C05005,
1232 <https://doi.org/10.1029/2006JC003514>, 2007.
- 1233 Witter, A., Lewis, B., and Luther, G. I.: Iron speciation in the Arabian Sea, *Deep-Sea Res. II*, 47, 1517–1539,
1234 [doi:10.1016/S0967-0645\(99\)00152-6](https://doi.org/10.1016/S0967-0645(99)00152-6), 2000.
- 1235 Wyrtki, K.: An equatorial jet in the Indian Ocean, *Science*, 181, 262–264,
1236 <https://doi.org/10.1126/science.181.4096.262>, 1973.
- 1237 Xie, P. and Arkin, P. A.: Global precipitation: A 17-year monthly analysis based on gauge observations, satellite
1238 estimates, and numerical model outputs, *B. Am. Meteorol. Soc.*, 78, 2539–2558, [https://doi.org/10.1145/1520-0477\(1997\)078<2539:GPAYAMA>2.0.CO;2](https://doi.org/10.1145/1520-0477(1997)078<2539:GPAYAMA>2.0.CO;2), 1997.
- 1240 Yang, X., Zhao, C., Yang, Y., and Fan, H.: Long-term multi-source data analysis about the characteristics of
1241 aerosol optical properties and types over Australia, *Atmos. Chem. Phys.*, 21, 3803–3825,
1242 <https://doi.org/10.5194/acp-21-3803-2021>, 2021.
- 1243 Zhang, Y., Rossow, W. B., Lacis, A. A., Oinas, V., and Mishchenko, M. I.: Calculation of radiative fluxes from
1244 the surface to top of atmosphere based on ISCCP and other global data sets: Refinements of the radiative transfer
1245 model and the input data, *J. Geophys. Res.*, 109, D19105, <https://doi.org/10.1029/2003JD004457>, 2004.
- 1246